

Atomic quantum simulation of a three-dimensional U(1) gauge-Higgs model

Yoshihito Kuno¹, Shinya Sakane², Kenichi Kasamatsu², Ikuro Ichinose¹, and Tetsuo Matsui²

¹*Department of Applied Physics, Nagoya Institute of Technology, Nagoya, 466-8555, Japan*

²*Department of Physics, Kindai University, Higashi-Osaka, 577-8502, Japan*

(Dated: December 3, 2024)

In this paper, we study atomic quantum simulations of a U(1) gauge-Higgs model on a three-dimensional (3D) spatial lattice. We start from an extended 3D Bose-Hubbard model with nearest-neighbor repulsions and show that it can simulate a U(1) gauge-Higgs model with next nearest-neighbor Higgs couplings. Here the phase of the boson variable on each site of the optical lattice describes the vector potential on each link of the gauge-model lattice. To determine the phase diagram of the gauge-Higgs model at a zero temperature, we perform Monte-Carlo simulations of the corresponding 3+1-dimensional U(1) gauge-Higgs model, and obtain the three phases, i.e., the confinement, Coulomb and Higgs phases. To investigate the dynamical properties of the gauge-Higgs model, we apply the Gross-Pitaevskii equations to the extended Bose-Hubbard model. We simulate the time-evolution of an electric flux initially put on a straight line connecting two external point charges. We also calculate the potential energy between this pair of charges and obtain the string tension in the confinement phase. Finally, we propose a feasible experimental setup for the atomic simulations of this quantum gauge-Higgs model in the 3D optical lattice.

PACS numbers: 03.75.Hh, 67.85.Hj, 11.15.Ha, 64.60.De

I. INTRODUCTION

In the last several years, quantum simulation has been one of the most actively studied subjects in physics [1]. Being stimulated by enormous progress in experiments on ultra-cold atomic systems, theoretical proposals for quantum simulations of various physical systems and associated phenomena have been made [2, 3]. Atomic quantum simulation of lattice gauge theories (LGT's) is one of them [4–16]. LGT was introduced by Wilson in 1974 [17] to study the mechanism of quark confinement in strong interaction. Since then, various models of LGT have been studied both analytically and numerically in various fields of physics including high energy physics [18], condensed matter physics [19], and neural networks [20], etc.

LGT is known to have three possible phases, confinement, Coulomb and Higgs phases [17, 18]. These phases and the phase transitions among them are crucial concepts in various scenes of physical phenomena. For LGT models with/without bosonic matter fields, the static equilibrium properties such as the phase diagram can be studied by the standard Monte-Carlo (MC) simulations. On the other hand, for LGT including a finite density of fermions, MC simulations generally suffer from the negative-sign problem, and no convincing methods to study the static properties are available. The atomic quantum simulation does not suffer from the negative-sign problem, and therefore its realization is strongly desired to understand LGT of fermions. Another and essential advantage of quantum simulation of LGT models (either with bosons or fermions) is its ability to simulate the real-time dynamics (time-development) of the system. Such simulations help us not only to study the dynamical properties, such as the transport phenomena, but also to intuitively understand the characteristics of

each of these three phases. For example, the spatio-temporal images of electric fluxes shall let us sensuously comprehend what happens in each phase.

In atomic quantum simulation of the LGT, implementation of the local gauge invariance, i.e., the Gauss-law constraint, is a key ingredient. For the pure compact U(1) LGT, i.e., theory of self interacting compact U(1) gauge fields without matter fields, the Gauss-law constraint is expressed by the operator identity $\vec{\nabla} \cdot \vec{E} = 0$, where \vec{E} is the electric field operator. Some proposals [4, 5] have appeared to implement this Gauss law in cold atom systems, which requires a particular limit of the strength of interactions between atoms [21]. This limit seems hard to achieve experimentally, but the available atomic systems without this limit certainly break the local gauge symmetry.

In the previous work [13], we pointed out and verified that this explicit breaking in the pure LGT can be interpreted as an effect of newly introduced charged matter field in *a new gauge theory including Higgs field*. Exact local gauge symmetry is respected in the way that the correct Gauss law holds as $\vec{\nabla} \cdot \vec{E} \propto$ (charge of Higgs field). Explicitly, we started with the so called extended BHM (EBHM), which is given by adding off-site repulsions to the BHM. We showed that a U(1) gauge-Higgs model (GHM) emerges naturally as a low-energy effective model of the EBHM when certain conditions for the parameters of EBHM are satisfied. There, the Higgs field $\phi(x)$ appears in the form of London limit, i.e., its radial fluctuations are frozen as $|\phi(x)| = 1$. In other words, the model discussed in Refs. [4, 5], which has an exact local gauge invariance only in the specific limit, can be viewed as a gauge fixed version of the GHM in the particular gauge $\phi(x) = 1$ (unitary gauge). This argument applies for the EBHM in arbitrary dimensions and without severe fine tunings of parameters.

Let us list up the relation between the original atomic model and the target gauge model studied in Ref. [13]. The atomic model is the EBHM on the 3D optical lattice (OL), and the effective gauge model at low energies is the GHM on the 3D lattice (let us call it the gauge lattice (GL)).

(A1) The site a of the OL is the midpoint of the link $(r, r + \hat{i})$ of the GL where r is the site of the GL and \hat{i} ($i = 1, 2, 3$) is the unit lattice vector in the positive i -th direction (See Fig. 1).

(A2) The phase $\hat{\theta}_a$ of the bosonic operator $\hat{\psi}_a = \exp(i\hat{\theta}_a)\sqrt{\hat{\rho}_a}$ for the bosons sitting on the site a is identified to the U(1) gauge field $\hat{\theta}_{r,i}$ on the link $(r, r + \hat{i})$. This guarantees the U(1) periodicity of the GHM (compactness) under $\hat{\theta}_{r,i} \rightarrow \hat{\theta}_{r,i} + 2\pi$. In LGT the electric field operator $\hat{E}_{r,i}$ is conjugate to the vector potential $\hat{\theta}_{r,i}$. The above identification implies that $\hat{E}_{r,i}$ corresponds to the amplitude operator $\sqrt{\hat{\rho}_a}$ of atoms.

(A3) We assumed that the density of atoms $\hat{\rho}_a$ has a uniform distribution in average, $\langle \hat{\rho}_a \rangle = \rho_0$, and its fluctuation $\hat{\eta}_a \equiv \hat{\rho}_a - \rho_0$ is small compared to ρ_0 , $\hat{\eta}_a/\rho_0 \ll 1$ at low energies. So we neglect higher-order terms than $O((\hat{\eta}_a/\rho_0)^2)$ in the effective action. In practice, these conditions may suggest $\rho_0 \gtrsim 10$, which is achieved in a relatively easy manner in experiments (See Sec. II for details). We stress that we *do not* assume the Bose-Einstein condensation (BEC) of cold atoms a priori; rather we are interested in a transition itself from a disordered incoherent state to a BEC, because a BEC transition corresponds to a confinement-deconfinement transition of gauge theory (See Sec. III).

Then the explicit relationship between the two models is established; the interaction parameters of the GHM are given by explicit functions of the parameters of the EBHM. In Ref.[13] we obtained the phase diagram of the corresponding (3+1)D U(1) GHM defined on the (3+1)D lattice [22] for some set of parameters. This phase diagram may be used as a guide for experimentalists to select parameters of the EBHM, i.e., parameters in experimental setups of quantum simulations. Recently, the EBHM has been realized for cold atoms on a 3D OL and some interesting experimental results have been reported [23]. We are looking forward to hearing further results of experimental studies, especially those which are relevant to LGT including the GHM studied in the present paper.

Let us comment that our way to introduce the U(1) gauge field by the points (A2) and (A3) is in strong contrast to another way [5–12] using the quantum link model (gauge magnet). The gauge-magnet recipe for U(1) gauge operator prepares a multiplet of boson states $|S_{az}\rangle$ at each site a with the multiplicity $2S + 1$, and uses the pseudo-spin formalism. There the electric field \hat{E}_a , is identified as $\hat{E}_a = \hat{S}_{az}$, and therefore the range of the eigenvalue $E_a = S_{az}$ is restricted to $(-S, S)$. To recover the expected genuine support of U(1) momentum operator $E_a \in \mathbf{Z}$ (integer) one needs to take the limit $S \rightarrow \infty$.

In our second paper[24], we focused on the EBHM in

the two-dimensional (2D) optical lattice and the resulting 2D GHM. A reason of choosing the 2D system is that it is easier to set up experimentally than the 3D system. We studied the following three points;

(B1) Phase diagram of the (2+1)D GHM as well as the EBHM itself, and found that the Coulomb phase is missing as expected from the study of the related models[25].

(B2) Formulation and solution of the Gross-Pitaevskii equation (GPE)[27] of the EBHM. GPE [28] is an approximate but useful equation describing the time-evolution of a quantum system. It has been widely applied mainly in condensed matter physics [27, 29].

(B3) Proposal of two feasible methods to set up a practical atomic simulator; one is based upon the excited bands of an optical lattice and the other uses dipolar atoms in a triple-layer optical lattice. These may help experimentalists to set up their systems of quantum simulation of LGT.

In this paper, we return to the 3D GHM again, and present a detailed account of the first paper [13]. Furthermore, we study the following three new aspects;

(C1) we refine and generalize the phase structure.

(C2) we extend the GPE study of dynamical properties made for the 2D GHM.

(C3) we propose a feasible experimental set up of a system describing the 3D GHM.

The structure of the paper is as follows. In Sec. II, we introduce the 3D EBHM, the BHM with nearest-neighbor repulsions and explain how the GHM appears as its effective model at low energies. In Sec. III, we discuss the results of MC simulations of the resultant GHM. The phase diagrams are shown and the physical properties of each phase are explained. The Higgs phase in gauge theory there corresponds to the superfluid phase of cold atoms, and the confinement phase corresponds to the Mott-insulator phase which has no phase coherence. In Sec. IV, we study the dynamical properties of the GHM by using the GPE. In particular, we are interested in the time evolution of an electric flux put on links of the gauge-model lattice. The electric flux behaves quite differently in the confinement and Higgs phases. String tension is also calculated. In Sec. V, we make a proposal for feasible experiment of the EBHM to simulate the GHM. The recipe starts from a system of two species of bosons (a and b atoms) and by changing over the optical-lattice structure to obtain a desired system consisting of the original a atoms. Sec. VI is devoted for conclusion.

II. FROM THE EXTENDED BOSE-HUBBARD MODEL TO THE U(1) GAUGE-HIGGS MODEL

In this section, we start from the EBHM that is to be realized by ultra-cold atom systems on an optical lattice and show that it is equivalent to the 3D GHM under certain conditions. For the optical lattice we choose the body-centered tetragonal (BCT) lattice where the unit

cell is a cuboid of the size $a_1 \times a_2 \times a_3$ with $a_1 = a_2 = a$ and $a_3 = \sqrt{2}a$. In Fig. 1, this BCT lattice is illustrated where the black circles denote its sites. These sites are the potential minima and atoms may sit on them (See Sec. V for details). In Fig. 1, we also draw the GL on which the GHM is defined. Its sites are shown by red squares in Fig. 1. The GL is a simple cubic lattice with the lattice spacing $\sqrt{2}a$, so the volume of unit cell $(\sqrt{2}a)^3$ is twice larger than that of the $a^2 \times \sqrt{2}a$. Every OL site sits on the midpoint of a NN pair of sites of the GL, i.e., it sits on a link of the GL. As long as one imposes (i) the 3D GL is simple cubic and (ii) a link of the GL corresponds to a site of the OL, the lattice structure of the OL is unique to be the BCT shown in Fig. 1.

The Hamiltonian of the EBHM on this BCT lattice is given by

$$H_{\text{EBH}} = - \sum_{a \neq b} J_{ab} \hat{\psi}_a^\dagger \hat{\psi}_b + \frac{V_0}{4} \sum_a \hat{\rho}_a (\hat{\rho}_a - 1) + \sum_{a \neq b} \frac{V_{ab}}{2} \hat{\rho}_a \hat{\rho}_b, \quad (1)$$

where a and b denote the sites of the BCT lattice (this a is of course different from the lattice spacing a above), $\hat{\psi}_a$ ($\hat{\psi}_a^\dagger$) is the annihilation (creation) operator of the bosonic atom at site a satisfying the canonical commutation relation $[\hat{\psi}_a, \hat{\psi}_b^\dagger] = \delta_{ab}$, and $\hat{\rho}_a = \hat{\psi}_a^\dagger \hat{\psi}_a$ is the atomic density. The parameter J_{ab} ($= J_{ba}$) is the hopping amplitude between the pair of sites a and b , V_0 and V_{ab} ($= V_{ba}$) are the on-site and off-site repulsions between atoms at a and (a, b) , respectively. We confine ourselves to the repulsive interactions $V_0 > 0$ and $V_{ab} > 0$ in this work.

The values of J_{ab} and V_{ab} are shown in Table I and Fig. 1. To explain it, it is useful to partition unit cells of the OL into “even”-column cells (as one with the center sites 7, 7_\pm in Fig. 1) and “odd”-column cells (as one with 8, 8_\pm), where each column of cells extends in the z -direction. Even and odd columns are distinguished by their signature $(-)^{x+y}$ and face each other alternatively as in a black-red checker board in the x - y plane.

The nearest-neighbor (NN) pairs in the BCT lattice of Fig. 1 have the distance a and consist of two types, NN1; the ordinary pairs connecting each corners in the x - y plane (as (1,2) in Fig. 1) and NN2; the pairs starting from each body-center site (as (1,7)) because of the choice $a_3 = \sqrt{2}a$. Then J_{ab} and V_{ab} have the nonvanishing values $J_{ab} = J, V_{ab} = \gamma^{-2}$ for NN1 in all the unit cells and for NN2 in all the even cells, and $J_{ab} = V_{ab} = 0$ for NN2 in all the odd cells. J_{ab} are truncated up to the NN pairs and $J_{ab} = 0$ for longer pairs.

The next-NN (NNN) pairs have the distance $\sqrt{2}a$, and are classified into two types; NNN1: the pair has a GL site at its mid point (such as (2,4) in Fig. 1), NNN2: the pair does not have a GL site at its mid point (such as (1,5)). Then, V_{ab} is nonvanishing; $V_{ab} = \gamma^{-2}$ for NNN1, while $V_{ab} = 0$ for NNN2. Here, V_{ab} are truncated up to the NNN pairs and $V_{ab} = 0$ for longer pairs.

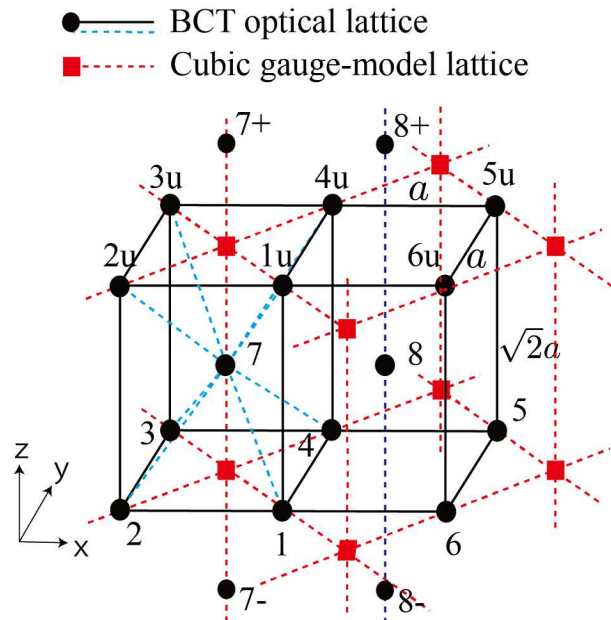


FIG. 1. (Color online) BCT optical lattice and cubic gauge-model lattice. The BCT lattice has the sites denoted by black circles and its unit cell is the cuboid of the size $a \times a \times \sqrt{2}a$. These sites are potential minima and cold atoms reside on them. The sites are labeled as 1, $1_u, 7_\pm$ where the suffixes refer to the relative location to the site labeled by 1 \sim 8. Red squares are the sites of the 3D GL on which the GHM is defined. It is a cubic lattice with the unit cell of the size $(\sqrt{2}a)^3$. Each black circles sits on the midpoint of a nearest-neighbor pair of red circles, i.e., sits on a link of the 3D GL.

These settings of parameters sound rather strange, e.g., some NN and NNN pairs have the same value $V_{ab} = \gamma^{-2}$ [30]. However, it is necessary to relate this EBHM to a model of LGT, and we present in Sec. V a feasible experimental way to set up an atomic system that describes the EBHM with this choice of parameters.

In order to derive the effective gauge field theory from H_{EBH} in Eq. (1), we introduce an operator corresponding to the phase degrees of freedom $\hat{\theta}_a$ of $\hat{\psi}_a$ as

$$\hat{\psi}_a = e^{i\hat{\theta}_a} \sqrt{\hat{\rho}_a}. \quad (2)$$

Then $\hat{\rho}_a$ and $\hat{\theta}_a$ are conjugate each other, satisfying the canonical commutation relation, $[\hat{\rho}_a, \hat{\theta}_b] = i\delta_{ab}$. We furthermore separate $\hat{\rho}_a$ into its mean value $\bar{\rho}_a$ and the quantum fluctuation $\hat{\eta}_a$ as

$$\hat{\rho}_a = \bar{\rho}_a + \hat{\eta}_a. \quad (3)$$

The value $\bar{\rho}_a$ may be estimated in various ways; some mean-field theory, more elaborated methods making use of self-consistency and/or numerical simulations. In this paper we consider the case in which a homogeneous state $\bar{\rho}_a = \rho_0$ (a -independent value) is realized. In Appendix A, we study a simple mean-field theory to determine $\bar{\rho}_a$ for the choice of Table I. We show there that inhomogeneous states competes in energy with the homogeneous

TABLE I. Atomic parameters J_{ab} and V_{ab} in Eq. (1) for the BCT optical lattice of Fig. 1. The parameters for pairs (a, b) that have longer distance than NNN are set zero. By this choice of parameters, the EBHM is capable to be equivalent to the 3D GHM. In particular, the group (iv) is responsible for Gauss law (See Eq. (7) below).

group	pairs in each group	(a, b)	J_{ab}	V_{ab}
(i)	NN1 and NN2 in the even unit cell (center site 7)	(1,2), (2,3), (3,4), (4,1), (1u,2u), (2u,3u), (3u,4u), (4u,1u), (1,7), (2,7), (3,7), (4,7), (1u,7), (2u,7), (3u,7), (4u,7)	J	γ^{-2}
(ii)	NN1 in the odd unit cell (center site 8)	(1,6), (6,5), (5,4), (4,1), (1u,6u), (6u,5u), (5u,4u), (4u,1u)	J	γ^{-2}
(iii)	NN2 in the odd unit cell (center site 8)	(1,8), (4,8), (5,8), (6,8), (1u,8), (4u,8), (5u,8), (6u,8)	0	0
(iv)	NNN1 with a mid-point GL site	(1,3), (2,4), (1u,3u), (2u,4u), (7,7+), (7,7-)	0	γ^{-2}
(v)	NNN2 with no mid-point GL site	(1,5), (4,6), (1u,5u), (4u,6u), (1,1u), (2,2u), (3,3u), (4,4u), (5,5u), (6,6u), (8,8+), (8,8-)	0	0

state, but for sufficiently large on-site repulsion V_0 compared to the inter-site repulsion γ^{-2} , the homogeneous state has lower energy as expected. For example, the homogeneous state is stable for $\gamma^{-2}/V_0 \lesssim 0.5$ for average atomic density per site $\sum_a \bar{\rho}_a / (\sum_a 1) = 10$. For the parameters which support the inhomogeneous state, one may still have a chance to obtain a lattice gauge model from the EBHM of Eq. (1). But for this purpose, the parameters J_{ab} and V_{ab} should be altered from the values in Table I to those that reflect nonuniformity of $\bar{\rho}_a$. In short, Gauss law relates not only J_{ab} and V_{ab} but also $\bar{\rho}_a$.

We identify each site a of the original BCT OL as a link $(r, i) \equiv (r, r + i)$ of the cubic GL on which the gauge model is defined, where $r = (x_1, x_2, x_3)$ is the site of the GL and $i = 1, 2, 3$ is the direction index (we use i also as the unit vector \hat{i}).

By setting $\bar{\rho}_a = \rho_0$, choosing the parameters in the Hamiltonian H_{EBH} in Eq. (1) as in Table I, and expanding the density operator in powers of $\hat{\eta}_a$ up to the second order, H_{EBH} of Eq. (1) becomes

$$H_{\text{EBH}}|_{\text{Table I}} = H'_{\text{EBH}} + O((\hat{\eta}/\rho_0)^3),$$

$$H'_{\text{EBH}} = \sum_r \left[\frac{1}{2\gamma^2} \left(\sum_k \hat{\eta}_k \right)^2 + \frac{V'_0}{2} \sum_k (\hat{\eta}_k)^2 - \rho_0 J \sum_{(m,n)} \cos(\hat{\theta}_m - \hat{\theta}_n) \right], \quad V'_0 \equiv V_0 - \frac{2}{\gamma^2}, \quad (4)$$

where r is the site of the GL, $k = 1, 2, 3, 4, 7, 7_{\pm}$ is the six OL sites surrounding r with the distance $a/\sqrt{2}$, and $(m, n) = (1,2), (2,3), (3,4), (4,1), (7,1), (7,2), (7,3), (7,4), (7_{\pm},1), (7_{\pm},2), (7_{\pm},3), (7_{\pm},4)$, are the twelve NN OL pairs surrounding r . We note that the condition of homogeneous state $\gamma^{-2}/V_0 \lesssim 0.5$ implies $V'_0 > 0$.

Let us make some comments on H'_{EBH} . As explained in Appendix A, the average value ρ_0 is adjusted so that no linear terms in $\hat{\eta}_a$ appear in H'_{EBH} . Further, straightforward expansion of H_{EBH} up to $O(\hat{\eta}^2)$ gives rise to an ex-

tra J -term $\propto J \hat{\eta}_m^\dagger \hat{\eta}_n \exp[i(\theta_m - \theta_n)] + \text{H.c.}$. We neglected this term because of the following reason. Our main interest is the BEC transition of cold atoms because this transition corresponds to the confinement-deconfinement transition in gauge theory (see Sec. III). Due to the limited accessibility to extremely low temperatures, the average density ρ_0 , which generally increases as the transition temperature rises, cannot be set arbitrary small, and one expects, e.g., $\rho_0 \gtrsim 10$ in practical experiments. Then the extra J term is to be neglected due to an extra suppression factor $\rho_0^{-1} (\lesssim 10^{-1})$ compared to the last ρJ -term in H'_{EBH} . We note that the coefficients γ^{-2}, V'_0 of the remaining two terms in H'_{EBH} should compete with $\rho_0 J$ near the phase transition, i.e., these three parameters are roughly of the same order. This point is confirmed a posteriori in the phase diagram Fig. 6 in Sec. III.

In the U(1) gauge theory, the vector potential $\hat{\theta}_{r,i}$ and the electric field $\hat{E}_{r,i}$ on the link (r, i) are a set of canonically conjugate operators satisfying $[\hat{E}_{r,i}, \hat{\theta}_{r',i'}] = -i\delta_{rr'}\delta_{ii'}$ [31]. They have the eigenvalues $\theta_{r,i} \in [0, 2\pi) \bmod(2\pi)$ and $E_{r,i} = 0, \pm 1, \pm 2, \dots \in \mathbb{Z}$ as mentioned in Sec. I. Therefore we make the following identification,

$$\hat{\theta}_{r,i} \equiv (-)^r \hat{\theta}_a, \quad \hat{E}_{r,i} \equiv -(-)^r \hat{\eta}_a, \quad (5)$$

where $(-)^r = (-)^{x_1+x_2+x_3}$ (we use the same letter θ both for OL and GL). It is straightforward to check that $\hat{\theta}_{r,i}$ and $\hat{E}_{r,i}$ are a canonical pair. The sign factor $(-)^r$ plays the crucial role to obtain the Gauss-law equation as seen below. At this stage, we stress that behaviors of electric field such as motion of electric fluxes are simulated by observing the density fluctuations of the EBHM experimentally.

By rewriting H'_{EBH} in Eq. (4) in terms of $\hat{\theta}_{r,i}, \hat{E}_{r,i}$ and sorting some terms suitably, we obtain the follow-

ing Hamiltonian of the GHM;

$$\begin{aligned}
H_{\text{GH}} &\equiv H'_{\text{EBH}} = \sum_r H_r \\
H_r &= \frac{1}{2\gamma^2} \left[\sum_i (\hat{E}_{r,i} - \hat{E}_{r-i,i}) \right]^2 + \frac{V'_0}{2} \sum_i \hat{E}_{r,i}^2 \\
&\quad - \rho_0 J \sum_{i < j} \left[\cos(\hat{\theta}_{r,i} - \hat{\theta}_{r,j}) + \cos(\hat{\theta}_{r,i} + \hat{\theta}_{r+i,j}) \right. \\
&\quad \left. + \cos(\hat{\theta}_{r+i,j} - \hat{\theta}_{r+j,i}) + \cos(\hat{\theta}_{r,j} + \hat{\theta}_{r+j,i}) \right]. \quad (6)
\end{aligned}$$

The first γ^{-2} -term in H_{GH} is just the rewriting of the first term of H'_{EBH} of Eq. (4) by using Eq. (5) as $\sum_k \hat{\eta}_k = \sum_i (\hat{E}_{r,i} - \hat{E}_{r-i,i})$. The last $\rho_0 J$ -term in H_{GH} comes from the NN hopping term of the EBHM, and represents the interaction between two phases put on the two links on the GL such as (r, i) and (r, j) . These two links have a common GL site (r) and make a right angle forming a shape of the letter L . The four terms in the square bracket represent the four such L -shapes, and they are four pieces contained in the plaquette $(r, r+i, r+i+j, r+j)$ of the GL. The relative signature between two phases are determined by the factor $(-)^r$ in Eq. (5)

In order to reveal that the system (6) can be regarded as a gauge system, let us see Eq. (6) term by term. The first term describes the Gauss law. In fact, due to its coefficient $(2\gamma^2)^{-1}$, the expectation value $E_{r,i}$ of $\hat{E}_{r,i}$ should satisfy

$$\left| \sum_i \nabla_i E_{r,i} \right| \lesssim \gamma, \quad \nabla_i E_{r,i} \equiv E_{r,i} - E_{r-i,i}. \quad (7)$$

We note $\sum_i \nabla_i E_{r,i}$ has the continuum limit $\propto \text{div} \vec{E}(r)$ as $a \rightarrow 0$. Equation (7) is the Gauss law on the GL with matter-field charge density $\propto \pm\gamma$. In path-integral formulation below (with the real time instead of the imaginary time), we shall identify this matter field a complex scalar field $\hat{\phi}_r$ (charged Higgs field) in the London limit. By taking the limit $\gamma^2 \rightarrow 0$, Eq. (7) reduces to $\sum_i \nabla_i \hat{E}_{r,i} = 0$, i.e., Gauss law without matter fields. The second term $\hat{E}_{r,i}^2$ is the well known energy density of the electric field [31]. The third term explicitly breaks the gauge invariance under the U(1) local gauge transformation,

$$\begin{aligned}
\hat{\theta}_{r,i} &\rightarrow \hat{\theta}'_{r,i} = \lambda_{r+i} + \hat{\theta}_{r,i} - \lambda_r, \\
\hat{E}_{r,i} &\rightarrow \hat{E}'_{r,i} = \hat{E}_{r,i}, \quad (8)
\end{aligned}$$

where λ_r is a real r -dependent parameter. However, as shown in the previous work [13], this term is closely related with a gauge invariant term. In fact, let us introduce a complex Higgs field $\hat{\phi}_r$ on the GL sites, and consider the hopping term of the Higgs field,

$$\begin{aligned}
H_3 &= -\frac{\rho_0 J}{2} \hat{\phi}_{r+i+j}^\dagger \hat{U}_{r+i,j} \hat{U}_{r,i} \hat{\phi}_r + \text{H.c.} + \dots, \\
\hat{U}_{r,i} &\equiv \exp(i\hat{\theta}_{r,i}), \quad (9)
\end{aligned}$$

where we used U(1) operator $\hat{U}_{r,i}$. The gauge transformation (8) for these operator is given by

$$\begin{aligned}
\hat{\phi}_r &\rightarrow \hat{\phi}'_r = V_r \hat{\phi}_r, \quad V_r \equiv \exp(i\lambda_r), \\
\hat{U}_{r,i} &\rightarrow \hat{U}'_r = V_{r+i} \hat{U}_{r,i} V_r^\dagger. \quad (10)
\end{aligned}$$

One may check easily that H_3 of Eq. (9) is invariant under the transformation (10).

Let us consider the Hamiltonian $\tilde{H}_{\text{GH}}(\hat{\phi})$ obtained from H_{GH} by replacing the third $\rho_0 J$ term by H_3 of Eq. (9). Then, by taking the so called London limit of the Higgs field in $\tilde{H}_{\text{GH}}(\hat{\phi})$, one ignores the radial fluctuation of $\hat{\phi}_r$, and sets $\hat{\phi}_r^\dagger \hat{\phi}_r = 1$, i.e., $\hat{\phi}_r$ has only the phase degree of freedom, $\hat{\phi}_r = \exp(i\hat{\varphi}_r)$. Furthermore, by fixing the gauge freedom under Eq. (10) to the so called unitary gauge, one may set $\hat{\phi}_x = 1$ (choose as $\lambda_r = -\varphi_r$). Then the resulting Hamiltonian is just H_{GH} itself, $\tilde{H}_{\text{GH}}(1) = H_{\text{GH}}$. That is, H_{GH} is viewed as a gauge fixed version of $\tilde{H}_{\text{GH}}(\hat{\phi})$ in the London limit. $\tilde{H}_{\text{GH}}(\hat{\phi})$ and $\tilde{H}_{\text{GH}}(1) = H_{\text{GH}}$ (in the London limit) have the same result for gauge invariant quantities including phase diagram, etc. We comment also that, as shown in Ref. [13], the first Gauss-law term in Eq. (6) naturally generates the Higgs coupling in the imaginary-time direction in the path-integral formalism of the gauge-Higgs model. We discuss it below.

The partition function of the quantum system H_{GH} of Eq. (6) on the GL at the temperature T is formulated by the path-integral method [17, 19]. To this end, we introduce the four-dimensional lattice by piling up 3D GLs along the imaginary-time ($\tau \in [0, \beta]$, $\beta \equiv (k_{\text{B}}T)^{-1}$) direction with the spacing $\Delta\tau$. We call this four-dimensional hypercubic lattice the 3+1D GL, and label its sites as $x = (x_0, r) = (x_0, x_1, x_2, x_3)$, with $x_0 = 0, 1, \dots, L_0$, $\Delta\tau = \beta/L_0$. To be precise, the limit $L_0 \rightarrow \infty$ should be taken [18]. However, in actual Monte Carlo simulations to determine the phase structure of LGT models, it is common to keep $\Delta\tau$ finite and draws useful results by applying scaling argument etc. [18]. We follow this approach in the next section.

Then the partition function of H_{GH} on the GL is given in the canonical formalism as follows,

$$\begin{aligned}
Z_{\text{GH}} &= \text{Tr} \exp(-\beta H_{\text{GH}}) = \int [DE_{x,i}] [D\theta_{x,i}] \\
&\quad \times \exp \left[\Delta\tau \left(i \sum_{x,i} E_{x,i} \dot{\theta}_{x,i} - \sum_{x_0} H_{\text{GH}}(\theta, E) \right) \right], \\
\int [DE_{x,i}] [D\theta_{x,i}] &= \prod_{x,i} \sum_{E_{x,i} \in \mathbf{Z}} \int_{-\pi}^{\pi} \frac{d\theta_{x,i}}{2\pi}, \\
\dot{\theta}_{x,i} &= \frac{1}{\Delta\tau} (\theta_{x+\hat{0},i} - \theta_{x,i}), \quad (11)
\end{aligned}$$

where $H_{\text{GH}}(\theta, E)$ is the c-number obtained by replacing the operators $\hat{\theta}_{r,i}$ and $\hat{E}_{r,i}$ in H_{GH} of Eq. (6) by their eigenvalues $\theta_{x,i}$ and $E_{x,i}$, respectively.

Below we sketch the way [13] to obtain the path integral expression of Z_{GH} in Lagrange formalism in terms

of the 4-component gauge field $\theta_{x,\mu} (\in [0, 2\pi])$ defined on the link $(x, x + \mu)$, where $\mu = 0, 1, 2, 3$ is the direction index (and the unit vector as before). First, we introduce the auxiliary field $\theta_{x,0}$, the 0-th component of the vector potential, put on the link $(x, x + \hat{0})$ in the 0-th direction of the 3+1D GL, to rewrite the term $-\Delta\tau\gamma^{-2}(\sum_i \nabla_i E_{x,i})^2/2$ in the exponent to $-\gamma^2\theta_{x,0}^2/(2\Delta\tau) + i\theta_{x,0}\sum_i \nabla_i E_{x,i}$ by the usual Gaussian integration, and replace $\theta_{x,0}^2$ by $2(1 - \cos\theta_{x,0})$ respecting the periodicity under $\theta_{x,0} \rightarrow \theta_{x,0} + 2\pi$, which is required by the $E_{x,i}$ -summation over $E_{x,i} \in \mathbf{Z}$.

At this stage, we note that the Gauss law shown in Eq. (7) is derived as the saddle point in the integration over $\theta_{x,0}$, i.e., at the level of averaged quantities in path integral. In fact, the saddle point of the $\theta_{x,0}$ -dependent term in the exponent with the imaginary time being replaced by the real time $t (= -i\tau)$ reads as

$$\begin{aligned} \frac{\partial}{\partial\theta_{x,0}} \left[i\frac{\gamma^2 \cos\theta_{x,0}}{\Delta t} + i\theta_{x,0} \sum_i \nabla_i E_{x,i} \right] &= 0 \\ \rightarrow \sum_i \nabla_i E_{x,i} = J_{x,0}, \quad J_{x,0} &= \frac{\gamma^2 \sin\theta_{x,0}}{\Delta t}. \end{aligned} \quad (12)$$

Next, we perform $\int [DE_{x,i}]$ by using the Poisson's summation formula to obtain a periodic Gaussian form, and making Villain's approximation to replace it by a cosine form. Z_{GH} is then expressed as follows;

$$\begin{aligned} Z_{\text{GH}} &= \int [D\theta_{x,\mu}] \exp(A_{\text{GH}}), \\ A_{\text{GH}} &= A_{\text{I}} + A_{\text{P}} + A_{\text{L}}, \\ A_{\text{I}} &= \sum_{x,\mu} c_{1\mu} \cos\theta_{x,\mu}, \quad A_{\text{P}} = \sum_{x,\mu < \nu} c_{2\mu\nu} \cos\theta_{x,\mu\nu}, \\ \theta_{x,\mu\nu} &\equiv \theta_{x,\mu} + \theta_{x+\mu,\nu} - \theta_{x+\nu,\mu} - \theta_{x,\nu}, \\ A_{\text{L}} &= \sum_{x,i < j} c_{3ij} [\cos(\theta_{x,i} - \theta_{x,j}) + \cos(\theta_{x,i} + \theta_{x+i,j}) \\ &\quad + \cos(\theta_{x+i,j} - \theta_{x+j,i}) + \cos(\theta_{x,j} + \theta_{x+j,i})], \end{aligned} \quad (13)$$

where $\nu = 0, 1, 2, 3$ and i and j ($= 1, 2, 3$) are spatial indices as before.

From H_{GH} in Eq. (6) and through the way to introduce scalar potential $\theta_{x,0}$, *non-vanishing coefficients* in Eq. (13) are listed up as follows;

$$\begin{aligned} c_1 &\equiv c_{10} = \frac{\gamma^2}{\Delta\tau}, \\ c_2 &\equiv c_{201} = c_{202} = c_{203} = \frac{1}{\Delta\tau V_0}, \\ c_3 &\equiv c_{312} = c_{313} = c_{323} = J\rho_0\Delta\tau. \end{aligned} \quad (14)$$

Therefore the effective action $A_{\text{GH}}(\theta_{x,\mu})$ has asymmetric couplings concerning to the space-time directions. This is in strong contrast with the LGT models in high-energy physics [17]. This is remarkable in the plaquette term A_{P} . The Wilson model [17] has $c_{2\mu\nu} = c_2$ while Eq. (14) shows that $c_{2ij} = 0$ for the plaquettes in the space-space directions. Here we note that there are some proposals

for generating the space-space plaquette interactions in the context of quantum simulation of LGT using cold atomic systems [4, 5, 33, 34] such as making use of the second-order perturbation theory assuming the L-shaped interaction in A_{L} a small perturbation. Therefore, we shall study the model not only of Eq. (14) but also with nonvanishing space-space plaquette terms ($c_{2ij} \neq 0$) in the following section.

We comment here on the gauge invariance in Lagrange formalism. A_{I} and A_{L} in the effective action $A_{\text{GH}}(\theta)$ break the gauge invariance under the 4D transformation, $\theta_{x,\mu} \rightarrow \lambda_{x+\mu} + \theta_{x,\mu} - \lambda_x$. However, one may introduce the gauge-Higgs action $\tilde{A}_{\text{GH}}(\theta, \varphi)$, which is *defined simply by the replacement* $\theta_{x,\mu} \rightarrow \theta_{x,\mu} - \varphi_{x+\mu} + \varphi_x$ in $A_{\text{GH}}(\theta)$ as $\tilde{A}_{\text{GH}}(\theta, \varphi) \equiv A_{\text{GH}}(\theta - \varphi + \varphi)$ (its explicit form is given in Eq. (11) of Ref. [13]). It is invariant under the combined gauge transformation,

$$\theta_{x,\mu} \rightarrow \lambda_{x+\mu} + \theta_{x,\mu} - \lambda_x, \quad \varphi_x \rightarrow \varphi_x + \lambda_x, \quad (15)$$

by construction. Then $A_{\text{GH}}(\theta)$ is just the gauge fixed version to the unitary gauge $\varphi_x = 0$; $A_{\text{GH}}(\theta) = \tilde{A}_{\text{GH}}(\theta, 0)$. At the level of partition function, there holds the equivalence,

$$\tilde{Z}_{\text{GH}} \equiv \int [D\theta_{x,\mu}] [D\varphi_x] \exp(\tilde{A}_{\text{GH}}(\theta, \varphi)) = Z_{\text{GH}}. \quad (16)$$

Some properties of the Higgs field may be drawn from the gauge-invariant action $\tilde{A}_{\text{GH}}(\theta, \varphi_x)$. For example, its A_{I} term reads as $c_{10}[\phi_{x+0}^* \exp(i\theta_{x,0})\phi_x + \phi_x^* \exp(-i\theta_{x,0})\phi_{x+0}]/2$. The first term describes propagation of a Higgs particle along the time axis in the positive direction as for an ordinary particle, whereas the second term describes its back propagation as for an antiparticle [19]. Therefore, the present Higgs particles are accompanied with their antiparticles having charges with the opposite sign. This is not strange at all although we treated the atoms described by the EBHM as totally nonrelativistic ones without their antiparticles. The Higgs charge density $J_{x,0}$ appearing in Eq. (12) is recalculated from the φ -dependent part of \tilde{A}_{GH} by $J_{x,0} = -\partial\tilde{A}_{\text{I}}(\theta, \phi)/\partial\theta_{x,0} = c_1 \sin(\theta_{x,0} - \varphi_{x+0} + \varphi_x)$, which is just the gauge-invariant version of Eq. (12). In a similar manner, the Higgs current density $J_{x,i}$ is calculated from the c_3 -term of the action $\tilde{A}_{\text{GH}}(\theta, \phi)$ as $J_{x,i} = -\partial\tilde{A}_{\text{L}}(\theta, \phi)/\partial\theta_{x,i} = \sum_j c_{3ij} \sin(\theta_{x,i} - \theta_{x,j}) + \dots$. The conservation law $\sum_\mu \nabla_\mu J_{x,\mu} = 0$ holds owing to the gauge invariance.

III. PHASE DIAGRAM OF THE U(1) GAUGE-HIGGS MODEL: MC SIMULATION

In the previous section, we explained how the 3D U(1) GHM of Eq. (6), or equivalently its path-integral expression (13) on the 3+1D lattice, appears from the EBHM of Eq. (1) in the 3D OL as its low-energy effective model. Therefore, various dynamical properties of this GHM are

to be ‘quantum simulated’ by the cold atomic gases in near future. On the other hand, its static properties such as the phase structure and correlation functions may be studied by various conventional techniques. Such static informations are certainly useful in understanding the model and also as guide to perform cold-atomic experiments.

In this section, we study the phase diagram of the 3D GHM by applying the standard (‘classical’) MC simulation to the 3+1D system of Eq. (13). This brings no difficulties such as the negative-sign problem because the system involves only bosonic variables and has a positive definite probability. In high-energy physics, the 3+1D U(1) gauge-Higgs model [17, 18] that is related with the present GHM has the symmetric couplings and is defined by Eq. (13) by setting $c_{1\mu} = c_1, c_{2\mu\nu} = c_2, c_{3ij} = 0$. Its phase diagram is known to have three phases, i.e., confinement, Coulomb, and Higgs phases [17, 19]. They are distinguished by the strength of fluctuations of $\theta_{x,\mu}$ as large, medium, small, respectively. Also, the potential energy $V(r)$ between two point sources being oppositely charged and separated by distance r has different typical behavior as $V(r) \propto r, 1/r, \exp(-mr)$, respectively.

Generally speaking, these three phases are distinguished by fluctuations of gauge field $\Delta\theta_{x,\mu}$ and fluctuations of Higgs field $\Delta\varphi_x$. Confinement phase has large $\Delta\theta_{x,\mu}$, Coulomb phase has small $\Delta\theta_{x,\mu}$ and large $\Delta\varphi_x$, and Higgs phase has small $\Delta\theta_{x,\mu}$ and $\Delta\varphi_x$. In the gauge fixed representation such as Eq. (13), $\Delta\varphi_x$ are not defined. In this case, one may measure averages and fluctuations of the Higgs-coupling terms such as A_I and A_L of Eq. (13) term by term. These may be used to judge whether the system is in the Higgs phase.

Because the present GHM has the asymmetric couplings $c_{1\mu}$ and $c_{2\mu\nu}$ in four directions and additional c_{3ij} couplings as shown in Eq. (14), its phase diagram should be examined separately, and we expect some richer phase structure.

To calculate the phase diagram, we measure the following ‘‘internal energy’’ U and the ‘‘specific heat’’ C as functions of the coupling constants;

$$\begin{aligned} U &= \langle A_{\text{GH}} \rangle / L^4, \\ C &= \langle (A_{\text{GH}} - \langle A_{\text{GH}} \rangle)^2 \rangle / L^4, \end{aligned} \quad (17)$$

where we consider the 3+1D space-time hypercubic lattice with the common linear size L_μ in the μ -th direction, $L_\mu = L$ with periodic boundary condition. We use the standard Metropolis algorithm [35] with typical sweeps $50000+10 \times 5000$ and calculate errors as the standard deviation of 10 samples. The thermodynamic limit is given by taking $L \rightarrow \infty$, which we shall discuss later together with the path-integral requirement $\Delta\tau \rightarrow 0$. We determine the order of phase transition by checking the behaviors of U and C as follows; (i) If U exhibits a hysteresis (a jump $\Delta U \neq 0$) as we changes a parameter back and forth, it is a first-order transition; (ii) If C has a peak increasing as L increases, it is a second-order transition; (iii) If U has no hysteresis and the peak is round or not

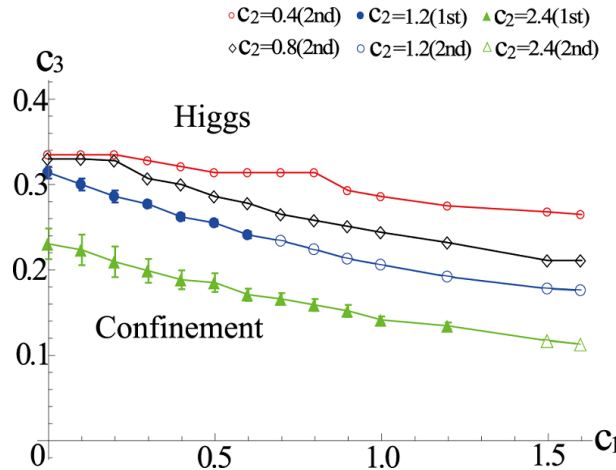


FIG. 2. (Color online) Phase diagram in the c_1 - c_3 plane for various values of c_2 calculated by Monte Carlo simulation of the 3+1D lattice of the size L^4 ($L = 16$). There exist the Higgs phase and the confinement phases, and they are separated by the first-order (1st) or second-order (2nd) phase-transition lines. The transition points are located from the peak of C for a 2nd-order transition and the midpoint of the hysteresis curve of U for 1st-order transition. Error bars for 1st-order transition indicate the size (starting and ending points) of hysteresis along the c_3 axis.

develops as L increases, it is a crossover (no genuine transition) [36].

In Fig. 2, we show the phase diagram in the c_1 - c_3 plane for several fixed values of c_2 . There are two phases. Below we shall see that the phase in the lower c_3 region is the confinement phase and the phase in the higher c_3 region is the Higgs phase. They are separated by a first-order or second-order phase transition line. In Fig. 3, we present two sets of U and C as functions of c_3 for fixed c_1, c_2 , which exhibit a typical second-order and first-order transition, respectively. For the first-order transitions, the hysteresis effect obscures the location of transition point. In Fig. 2, we plot the midpoint of the hysteresis curve as the transition point. For precise determination of the transition point, we need other algorithm such as the multicanonical ensemble [37], which is a future problem.

To identify the nature of the two phases in Fig. 2, we measure the fluctuations (uncertainty) ΔE of electric field \vec{E} and the fluctuation ΔB of magnetic field \vec{B} . Explicitly we use the following quantities;

$$\begin{aligned} W_e &\equiv \frac{1}{3L^4} \sum_{x,i} \langle (E_{x,i} - \langle E_{x,i} \rangle)^2 \rangle \\ &= \frac{1}{3L^4} \sum_{x,i} \left[c_2 \langle \cos \theta_{x,0i} \rangle - c_2^2 \langle \sin^2 \theta_{x,0i} \rangle \right], \end{aligned} \quad (18)$$

$$W_m \equiv \frac{1}{3L^4} \sum_{x,i < j} \langle \sin^2 \theta_{x,ij} \rangle, \quad (19)$$

where $\theta_{x,\mu\nu}$ is defined in Eq. (13). In Eq. (18), the second equality is obtained by following the path from Eq. (11)

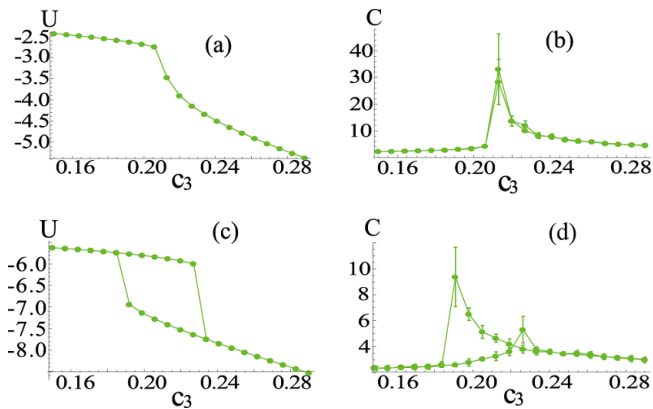


FIG. 3. (Color online) Typical behaviors of the internal energy U and the specific heat C of Eq. (17) for $L = 16$. (a) U and (b) C for $c_1 = 0.9, c_2 = 1.2$ show a second-order phase transition at $c_3 \simeq 0.21$. (c) U and (d) C for $c_1 = 0.2, c_2 = 2.4$ show a first-order phase transition at $c_3 \simeq 0.185 \sim 0.235$. The hysteresis loop in (c) is obtained as we increases c_3 and then decreases it.

to Eq. (13) by adding the source term for $E_{x,i}$ to the action. The definition W_m of Eq. (19) is natural since the relation $\theta_{r,ij} \propto \sum_k \epsilon_{ijk} B_k(r)$ (ϵ_{ijk} is the completely anti-symmetric tensor) holds in the continuum limit [17, 18, 31] and $\sin^2 \theta$ is a simple compactification of θ^2 . There hold the correlations that large W_m implies large ΔB and $\Delta \theta_{x,i}$, large W_e implies large ΔE and *small* $\Delta \theta_{x,0}$ because $\theta_{x,0}$ is the Lagrange multiplier for the Gauss law $\sum_i \nabla_i E_{x,i} \simeq (-\gamma, \gamma)$. From the characterization of each phase given above, the confinement phase has small ΔE and large ΔB , while the Higgs phase and Coulomb phase have small ΔB and large ΔE .

In Fig. 4, we show W_e and W_m for the parameters chosen in Fig. 3. In the phase with smaller c_3 , W_e (W_m) is small (large). Hence, this phase is the confinement phase. On the other hands, since W_e (W_m) is large (small) in the phase with larger c_3 , this phase can be the Higgs or Coulomb phase. Because larger c_3 implies that the c_3 Higgs-coupling term A_L has larger expectation value and smaller fluctuations than the confinement phase at smaller c_3 , it should be the Higgs phase. This conclusion is confirmed by measuring $\langle A_L \rangle$ and the c_3 specific heat $(\Delta A_L)^2 \equiv \langle A_L^2 \rangle - \langle A_L \rangle^2$ directly.

The characteristics of the confinement phase, i.e., largeness of ΔB , is sometimes rephrased as a condensation of magnetic monopoles [25]. Magnetic monopoles describe topologically nontrivial configurations of the magnetic field strength $\theta_{x,ij}$, i.e., such configurations having “large” $\theta_{x,ij}$. To defined the monopole density Q_x , we decompose $\theta_{x,ij}$ into its *integer (large) part* $2\pi n_{x,ij}$ ($n_{x,ij} \in \mathbf{Z}$) and the remaining (small) part $\tilde{\theta}_{r,ij}$ as

$$\theta_{x,ij} = 2\pi n_{x,ij} + \tilde{\theta}_{x,ij}, \quad (-\pi < \tilde{\theta}_{r,ij} < \pi), \quad (20)$$

where $n_{x,ij} (\neq 0)$ describes nothing but the Dirac string (quantized magnetic flux) penetrating the plaquette

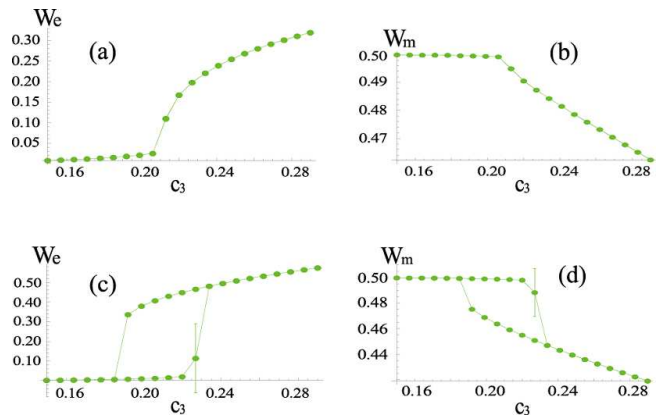


FIG. 4. (Color online) The fluctuation strength of electric and magnetic field, W_e and W_m of Eqs. (18) and (19) for $L = 16$. Panels (a) and (b) show W_e and W_m , respectively, for $c_1 = 0.9$ and $c_2 = 1.2$, while, (c) and (d) show those for $c_1 = 0.2$ and $c_2 = 2.4$. W_e is small (large) in the smaller (larger) c_3 region, whereas W_m behaves the other way around. From their behaviors, we can identify the confinement and Higgs phases as in the phase diagram in Fig. 2.

(x, ij) . Then, the monopole density Q_x is defined [38] as

$$\begin{aligned} Q_x &\equiv -\frac{1}{2} \sum_{i,j,k} \epsilon_{ijk} (n_{x+i,j,k} - n_{x,jk}) \\ &= \frac{1}{4\pi} \sum_{i,j,k} \epsilon_{ijk} (\tilde{\theta}_{x,jk} - \tilde{\theta}_{x,jk}), \end{aligned} \quad (21)$$

where the last equality comes from the identity $\sum_{i,j,k} \epsilon_{ijk} (\theta_{x+i,jk} - \theta_{x,jk}) = 0$ (lattice version of $\text{div-rot} = 0$). Therefore, Q_x measures the total magnetic fluxes emanating from 6 surfaces (plaquettes) of the 3D cube centered at the dual lattice site $x + \frac{1}{2} + \frac{2}{2} + \frac{3}{2}$. Q_x certainly expresses the magnitude of the topologically non-trivial fluctuations of space-component of the gauge field $\theta_{x,i}$ in a local and gauge-invariant manner. In Fig. 5, we plot the average $Q \equiv \langle Q_x \rangle$ for the two cases shown in Figs. 3 and 4. It has the similar behavior as W_m of Fig. 4; Q is large in the confinement phase and very small in the Higgs phase as expected.

To understand the phase structure of the GHM, let us focus on the order of phase transitions in Fig. 2. It may be summarized as follows; as c_3 increases while c_1 and c_2 being fixed, the transition from the confinement phase to the Higgs phase is second order for large c_1 and small c_2 and shifts to first order as c_1 decreases and/or c_2 increases. This crossover of the order is an interesting phenomenon itself. One may conceive a few plausible arguments to explain this point. Although it is not rigorous, we present such an argument in Appendix B. It is based on known facts on the related models and interpretation of the system (13) as a sum of mutually interacting two XY spin systems; one system has the action A_1 of Eq. (13) and consists of the time-component

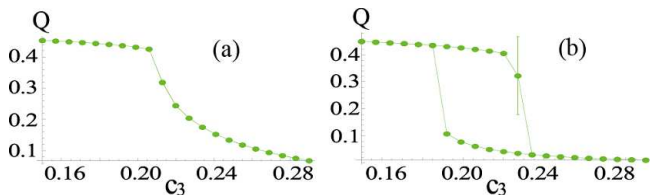


FIG. 5. (Color online) Magnetic monopole density $Q \equiv \langle Q_x \rangle$ [See Eq. (21)] for $L = 16$; (a) $c_1 = 0.9, c_2 = 1.2$, and (b) $c_1 = 0.2, c_2 = 2.4$. They have similar behaviors as the corresponding W_m in Fig. 4.

of gauge field $\theta_{x,0}$ and the other system has the action A_L of Eq. (13) and consists of space-component $\theta_{x,i}$. A synthetic effect between these two systems driven by the coupling action A_P of Eq. (13) may convert an ordinary second-order transition to a first-order one. This is one of the characteristics of the present system having asymmetric couplings in the space-time directions, which reflects the nonrelativistic nature of the starting EBHM. This is in strong contrast to the LGT studied in high-energy physics [17], which has symmetric couplings in the space-time directions reflecting the relativistic invariance.

At this point, we mention the possibility of the Coulomb phase in our system. A typical example of the Coulomb phase is the ordered phase of $\theta_{x,\mu}$ in the 4D Wilson model ($c_{1\mu} = c_{3\mu\nu} = 0, c_{2\mu\nu} = c_2$) for $c_2 \gtrsim 1.0$. For the symmetric 4D U(1) GHM ($c_{1\mu} = c_1, c_{2\mu\nu} = c_2, c_{3\mu\nu} = 0$), it appears in the region of large c_2 and small c_1 (it is a smooth extension from the Coulomb phase of the Wilson model). It is also known that the 3D Wilson model has only the confinement phase and no Coulomb phase [25]. In our system, because the spatial-spatial plaquette term is missing, $c_{2ij} = 0$, one may give up the Coulomb phase. However, the argument in Appendix B suggests that, for sufficiently large c_2 , both $\theta_{x,0}$ and $\theta_{x,i}$ may be stabilized to give rise to the Coulomb phase even without c_{2ij} . In fact, from some preliminary MC calculations such a possibility emerges for $c_2 \gtrsim 3.5$ at $c_1 = c_2 = 0$ (Note that the largest value of c_2 in Fig. 2 is $c_2 = 2.4$). We shall come back to this interesting point in future publications. Also we comment here on the approach in Ref. [5]. It is argued there in the context of the gauge magnet that the second-order perturbation of small c_{3ij} term may generate the c_{2ij} term effectively, but the present argument and Fig. 2 indicate that such c_{2ij} is not large enough to generate the Coulomb phase.

Now we turn to taking the limit of $\Delta\tau \rightarrow 0$ which is required in the precise path-integral treatment. This is important to use the present MC result such as the phase diagram Fig. 2 as a guide to set up experiments and interpret their results. For practical Monte Carlo simulations, as mentioned in Sec. II, we use sufficiently large but finite size L_0 in the imaginary-time direction with the finite-size scaling hypothesis, which, in our symmetric choice $L_\mu = L$, implies the thermodynamic limit

at the same time. We are interested in sufficiently low temperature region $T < T_{\text{BH}}$ where $T_{\text{BH}} \sim$ may be of $O(10 \text{ nK})$ by setting the parameters of H_{EBH} suitably to focus on quantum phase transitions instead of thermal phase transitions. This temperature region $T \simeq 0$ is consistent with our choice $L_\mu = L$ [17, 18]. Eq. (14) shows that the limit $\Delta\tau \rightarrow 0$ with the physical parameters $\gamma^{-2}, V'_0, J, \rho_0$ kept finite implies that the dimensionless parameters shrink to the limit $c_1, c_2 \rightarrow \infty, c_3 \rightarrow 0$ in the space of c_i . To discuss the possible phase transition, etc., we need to enlarge this limiting point in some way. This is possible by following the general procedures; (i) preparing the results of U and C at sufficiently large but finite L 's such that they exhibit scaling behaviors, and (ii) exploring the phase structure in a multi-dimensional space of new parameters which are $\Delta\tau$ -independent combinations composed from the original $\Delta\tau$ -dependent parameters.

We expect that one can get a single universal curve for phase boundary in the diagram with $\Delta\tau$ -independent parameters. As an example of this program, we redraw in Fig. 6 the phase structure of Fig. 2 in the two-dimensional plane of the horizontal axis; $c_1/c_2 = \gamma^2 V'_0$ and the vertical axis $c_2 \cdot c_3 = J\rho_0/V'_0$ [Fig. 6(a)] and $c_1 \cdot c_3 = \gamma^2 J\rho_0$ [Fig. 6(b)]. We note that the dimensions of parameter space reduce as 4 (original; $\gamma^2, J, \rho_0, \Delta\tau$) \rightarrow 3 (dimensionless; c_1, c_2, c_3) \rightarrow 2 ($\Delta\tau$ -eliminated; $c_1/c_2, c_2(c_1) \cdot c_3$).

In Figs. 6(a) and (b), it seems that the four lines do not merge to an expected universal curve. Further observation shows that the second order points for $c_2 = 0.8, 1.2, 2.4$ are relatively united to form a group, but the following two sets (i) and (ii) deviate from it; (i) the first-order points for $c_2 = 1.2, 2.4$ in Fig. 6(a) (although this is not so striking in Fig. 6(b)), and (ii) the second-order line for $c_2 = 0.4$ in Figs. 6(a) and (b). Possible explanation of this breach of discipline may be as follows; for set (i), first-order transitions often exhibit nonuniversal critical behaviors such as nonunique continuum (scaling) limit, which is in strong contrast to the universal behaviors of second-order (continuous) transitions, and for set (ii), $c_2 = 0.4$ is too small to consider the scaling region of $\Delta\tau \rightarrow 0$ because of $c_2 \propto (\Delta\tau)^{-1}$. In Ref. [24], we have made a similar redrawing of the phase diagram for the 2D GHM obtained from the 2D EBHM. There, several lines for different values of parameters (in fact same c_2 as here) merge rather well to a universal curve. We note that there are second-order transitions and crossovers but no first-order ones. Furthermore the line $c_2 = 0.4$ there merges to the universal line, but it is clear that the lowest qualified value of c_2 for scaling depends on the dimensionality of system.

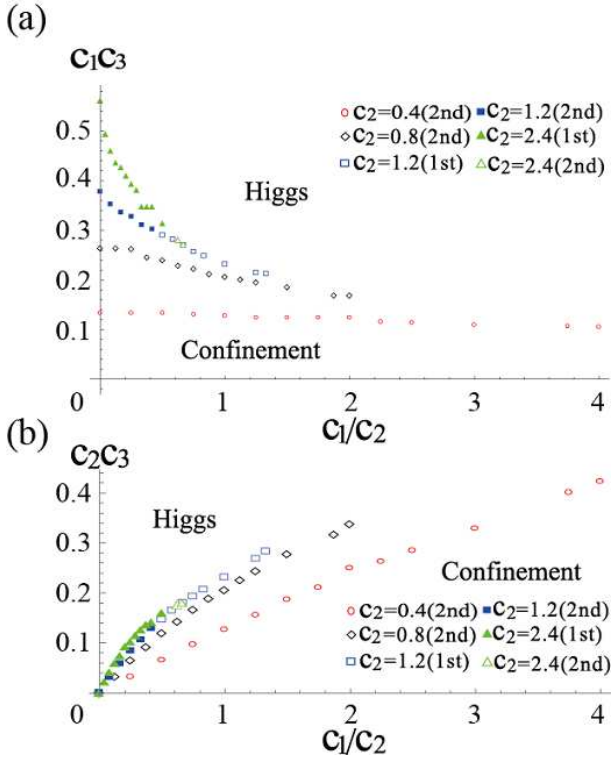


FIG. 6. (Color online) Phase diagrams for various values of c_2 , shown in Fig. 2, are redrawn in the planes of dimensionless coordinates; (a) c_1/c_2 - $c_2 \cdot c_3$ plane and (b) c_1/c_2 - $c_1 \cdot c_2 \cdot c_3$ plane. In terms of the original parameters, they read $c_1/c_2 = \gamma^2 V'_0$, $c_2 \cdot c_3 = J\rho_0/V'_0$, $c_1 \cdot c_3 = \gamma^2 J\rho_0$.

IV. DYNAMICS OF ELECTRIC FLUX BY SEMICLASSICAL APPROXIMATION OF THE GAUGE-HIGGS MODEL

In the previous section, we obtained the phase diagram of the effective gauge system by the MC simulation in Figs. 2 and 6, which is one of the most important static properties of the system under question. In this section, we study dynamical properties of each phase in this phase diagram; in particular, we are interested in behaviors of an electric flux connecting a pair of external charges.

It is a challenging problem for exploring real-time dynamics of quantum many-body systems. Recently, tensor network method was applied to study the real time dynamics of string breaking for 1+1D quantum link model [39], but this method is restricted to the problems for one spatial dimension. Here, we use simple mean field treatment to study the real time dynamics by following our previous studies [24, 41], in which the semiclassical GPE (discrete nonlinear Schrödinger equation) was employed to study the dynamics of an electric flux in the GHE

derived from atomic system. We note that direct derivation and application of GPE for gauge theories including LGT is not straightforward due to the existence of gauge invariance; one needs to determine how to respect gauge invariance. The EBHM-GHM correspondence we explained so far offers us a convincing approach; one can derive and solve the GPE of the EBHM and use the correspondence in the two sets of parameters to interpret the solution in the context of the gauge theory.

The Gross-Pitaevskii description associated with the EBHM may be effective if the site occupation is large enough and the phase coherence in each site is well established, because the field operator at each site is just replaced by the c -number field within the GPE [26]. As explained before, this regime is within our assumption for realizing the GHM. More precisely, the Higgs phase can be described well by the GPE, because it corresponds to superfluid phase. As we approach the confinement phase, the GPE cannot work well to study the dynamics, because quantum fluctuation becomes large. However, we still expect that some qualitative feature can be captured by the Gross-Pitaevskii approach, as described in the previous studies [24, 41] and the later discussion. Quantum fluctuations can be included under some treatment, known as truncated Wigner approximation (TWA) [40], which is obtained by taking into account quantum fluctuations around the classical path up to the second-order. TWA consists of (i) deriving an equation of motion of the average value of quantum operator, which is just the GPE itself, and (ii) solving GPE for a given initial condition, and (iii) averaging over solutions of GPE with different initial conditions with a certain weight. The faithful treatment according to TWA requires the step (iii), which seems certainly important because $\hat{E}_{r,i}$ and $\hat{\theta}_{r,i}$ are canonically conjugate pairs and their averages should obey the uncertainty principle. Implementation of the requirement of the step (iii) into actual experiments and the discussion of appropriateness of the result with a single initial condition is discussed quantitatively for the system of GHM in one spatial dimension [41]. We leave these discussion for the present 3D model as a future problem, and focus on the detailed study with the most interesting initial condition below, which is certainly important by itself.

The equation of motion for the effective gauge model, GHM of Eq. (6), involves the expectation values $E_{r,i}(t)$ and $\theta_{r,i}(t)$ (t is the time) of the operators $\hat{E}_{r,i}$ and $\hat{\theta}_{r,i}$ of Eq. (5), respectively. It may be obtained by averaging the Heisenberg equations of motion for the operators $\hat{E}_{r,i}$ and $\hat{\theta}_{r,i}$ and truncating quantum correlations among them or by taking the saddle point configuration of the path integral in canonical formalism (11). Explicitly, we have

$$\begin{aligned}
\hbar \frac{d}{dt} E_{r,i} &= 2J\rho_0 \sum_{j=1,2,3(\neq i)} [\sin(\theta_{r,i} - \theta_{r,j}) + \sin(\theta_{r,i} + \theta_{r-j,j}) + \sin(\theta_{r,i} + \theta_{r+i,j}) + \sin(\theta_{r,i} - \theta_{r+j-j,j})] \\
\hbar \frac{d}{dt} \theta_{r,i} &= -V'_0 E_{r,i} - \frac{1}{\gamma^2} \left[E_{r,i} - E_{r-i,i} + \sum_{j=1,2,3(\neq i)} (E_{r,j} - E_{r-j,j}) \right] \\
&\quad - \frac{1}{\gamma^2} \left[-E_{r+i,i} + E_{r,i} + \sum_{j=1,2,3(\neq i)} (-E_{r+i,j} + E_{r+i-j,j}) \right], \tag{22}
\end{aligned}$$

for a canonically conjugate pair $\theta_{r,i}$ and $E_{r,i}$. These equations correspond to the discrete GPE, linearized only by the amplitude degree of freedom. We are interested in a motion of an electric flux initially pinned up between two external static source charges. Therefore, we confine ourselves to the solution of Eq. 22 with the initial condition representing such a situation.

We solve Eq. (22) by the standard Crank-Nicolson method with a discrete time step Δt . We use a 3D cubic lattice (GL) with the size $100 \times 100 \times 100$, i.e. we define the lattice site $r = (r_x, r_y, r_z)$ with $1 \leq r_i \leq 100$, and apply the Neumann boundary condition. Concerning to the dimensionless time step, we use $\Delta \tilde{t} \equiv V'_0 \Delta t / \hbar$ and set $\Delta \tilde{t} = 0.01$, and make runs with typical elapsed time steps $20000 \sim 30000 (\times \Delta \tilde{t})$. The realistic time scale corresponding to this choice can be estimated as $\Delta t = 0.01 \times \hbar / V'_0 \sim 0.0032$ msec for the typical energy scale $V'_0 / \hbar \sim 500$ Hz used in experiments [43]. For other dimensionless parameters we consider the case of $\tilde{\gamma}^2 \equiv \gamma^2 V'_0 = 1$ and 10, and $\tilde{J} \equiv J\rho_0 / V'_0 = 0.001 - 10$. These parameters correspond to $c_1/c_2 = \tilde{\gamma}^2$ and $c_2 \cdot c_3 = \tilde{J}$ in Fig. 6(a). For example, as \tilde{J} increases from 0.001 to 10 for $\tilde{\gamma}^2 = 1$, the system moves from the deep confinement region to the deep Higgs region in the phase diagram of Fig. 6(a).

As the initial condition of Eq. (22), we assume to put a plus charge at the site $r_+ = (50 - \ell/2, 50, 50)$ and a minus charge at the site $r_- = (50 + \ell/2, 50, 50)$, where ℓ is the distance between the external charges. Because there are not dynamical variables at the site in Eq. (22), we fix $E_{r_+,1} = 0.1$ ($E_{r_-,1} = 0.1$), corresponding to the electric field emitted from (absorbed to) the plus (minus) charge. Furthermore, along the straight line between the site r_+ and the site r_- , we set $E_{r,i} = E_0 = 0.1$ as the initial condition, which represents the connected electric flux. To study the stability of the electric flux, we measure fluctuations of the electric field (fluctuation of atomic density) by using the quantity;

$$\sigma(t) \equiv \sum_{(r,i) \in r_+ - r_-} \left[(E_{r,i}(t))^2 - E_0^2 \right]^2, \tag{23}$$

where the summation is taken for only sites along the straight line from the site r_+ to the site r_- , at which the initial electric flux is present. If the initial flux configuration is stable for a long time, $\sigma(t)$ should take nearly zero.

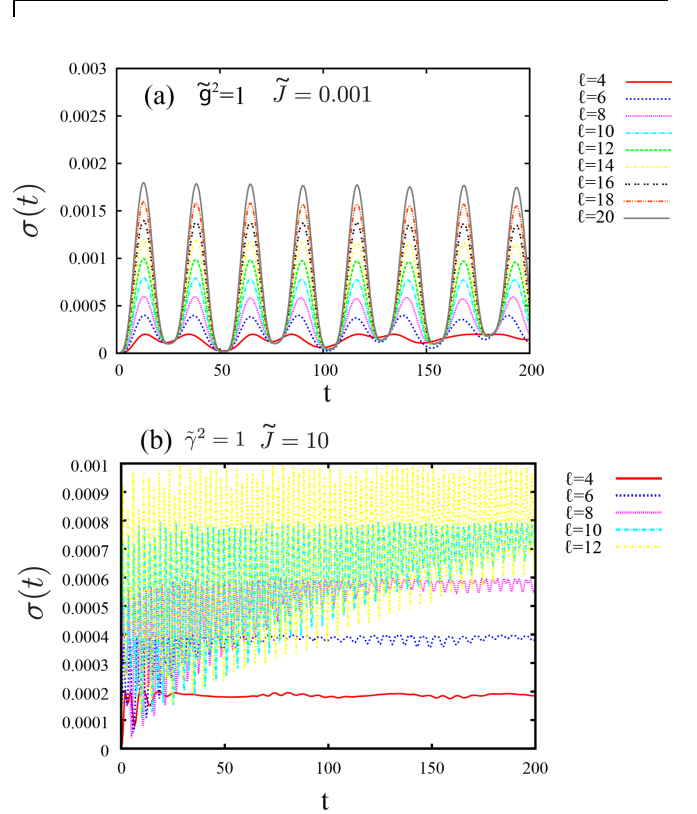


FIG. 7. (Color online) Time evolution of $\sigma(t)$ of Eq. (23) for various lengths ℓ of electric flux. In (a) for $\tilde{J} (\equiv J\rho_0/V'_0) = 0.001$ (confinement), $\sigma(t)$ continues oscillations and shows the stability of the electric flux. In (b) for $\tilde{J} = 10$ (Higgs), the oscillation of $\sigma(t)$ gradually disappears and the values of $\sigma(t)$ approach to an ℓ -dependent constant.

In the upper panel of Fig. 7, we show the time development of $\sigma(t)$ in the deep confinement phase ($\tilde{J} = 0.001$) for some flux lengths ℓ . The results indicates that $\sigma(t)$ exhibits an approximately periodic oscillation that makes almost complete recurrence to the initial state. This recurrence is more remarkable as the flux length ℓ is increased. The oscillating behavior of $\sigma(t)$ in time comes from the weak Higgs coupling that is present even for the present case and breaks a part of the electric flux and then undoes it. This phenomenon is similar to the string-antistring oscillation in the Schwinger mechanism [42], being also seen in the previous literature [24, 39, 41]. The “classical” MC simulations, which calculate the en-

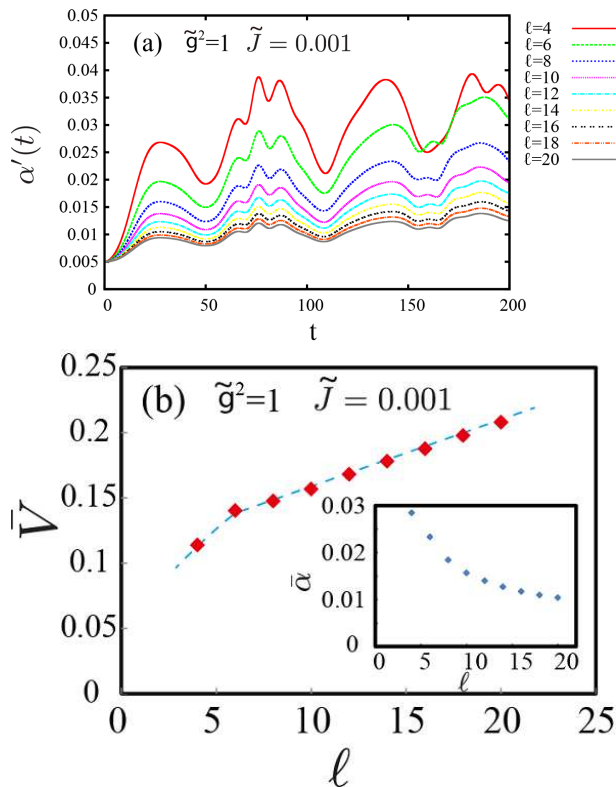


FIG. 8. (Color online) (a) Time evolution of the string tension α' of Eq. (24) for various lengths ℓ of electric flux. (b) Time average $\bar{V}(\ell)$ of the potential $V(\ell)$ and time average $\bar{\alpha}$ of α' with the time interval from $t = 0$ to $t = 200$. It is obvious that $\bar{\alpha}$ exhibits a smooth behavior converging to a constant as ℓ increases.

semble (time) average of physical quantities, cannot reveal this behavior of the electric flux in the confinement phase. We thus conclude that the electric flux is stable for a long time in the present parameter, which is the most important evidence to show that the system stays in the confinement phase, as we expected from the phase diagram by the MC simulation in Fig. 2.

On the other hand, Fig. 7 (b) shows the time development of $\sigma(t)$ in the deep Higgs phase with $\tilde{J} = 10$. The oscillating behaviors are gradually lost and tend to approach a constant value for any flux length ℓ . From the definition of $\sigma(t)$, this indicates the decay of the electric flux structure, because the finite constant value of $\sigma(t)$ means that the fraction of the electric field is dispersed from the initial rectilinear position between two charges put on the sites r_+ and r_- . In this case, the Higgs terms $\cos(\hat{\theta}_{r,i} - \hat{\theta}_{r,j})$ dominate over the electric term $\hat{E}_{r,i}^2$ in Eq. (6) for large J , and therefore the ‘condensation’ of the gauge potential takes place there.

In the confinement phase, it is interesting to measure the confinement potential between the external charges. In the confinement phase of LGTs without couplings to matter fields in the fundamental representation of the gauge group, the potential energy $V(\ell)$ of a pair of exter-

nal charges separated with a distance ℓ is well fitted by a linear rising confining potential, i.e., $V(\ell) = \alpha'\ell$, where α' is called string tension. It may be expected that the coupling to matter field in the fundamental representation changes the confinement potential to a short-range one because of the shielding effect. However the above observation of $\sigma(t)$ suggests that the confinement potential survives even in the presence of the Higgs field. In fact, from the result of $\sigma(t)$ in Fig. 7 (a), our calculation for small $\tilde{J} < 1$ is expected to represent the confinement phase; the shape of the electric flux as a initial state is present in a stable manner during the time evolution. Therefore, it is worthwhile to pursue the confining potential between static charges for such a case. For this purpose, we measure the total energy $W(\ell)$ of the configuration with the electric flux of the length ℓ , and define the potential energy $V(\ell)$ and the string tension α' as

$$V(\ell) = W(\ell) - W(0),$$

$$\alpha' = \frac{V(\ell)}{\ell}. \quad (24)$$

In Fig. 8 (a), we show the time evolution of α' for various ℓ 's. Because we force to put the two external charges at r_+ and r_- during the simulations, the total energy $W(\ell)$ is not a constant of motion, and α' thus exhibits an oscillating behavior, as seen in Fig. 8 (a). In Fig. 8 (b), we thus take a time average of α' , showing the time averaged values $\bar{\alpha}$ as well as $\bar{V}(\ell)$. It is obvious that the time average $\bar{\alpha}$ monotonically decreases and tends to be constant as ℓ increases. As a result, the potential exhibits an expected linear behavior $V(\ell) \propto \ell$, which strongly supports that the present system is in the confinement phase.

Note that the short distance behavior for $\ell < 5$ in Fig. 8 deviates from the linear dependance. This may come from the perturbative one-photon exchange effect that gives rise to the Coulomb potential like $V(\ell) \propto -\frac{1}{\ell}$, although the vacuum polarization by the Higgs field renormalizes the external charges. For small ℓ , the confining potential becomes weak even for the confinement phase. Thus, the effect of the confinement does not emerge significantly. This behavior can be seen in the data $\ell = 4$ of Fig. 7, in which we cannot discriminate the behaviors of σ between (a) and (b). This might imply that there emerges an *asymptotic freedom* which makes the behaviors less distinctive between the Higgs and confinement phases.

Finally, in Fig. 9 we show the 3D electric field $E_{r,i}$ and the divergence $\text{div}\mathbf{E}_r \equiv \sum_i \nabla_i E_{r,i}$. The upper panels in Fig. 9 represent the snapshots of electric field $E_{r,i}$ at $t = 200$ for the typical parameter values, $J = 0.001$ (confinement) and $J = 10$ (Higgs), where we measured the electric field in the vicinity of the initial electric flux. These results represent the intuitive picture expected from the LGT; the electric flux between static charges survives in the confinement phase; while, it breaks off in Higgs phase. In the lower panels of Fig. 9, we show the snapshots of the divergence of the 3D electric field

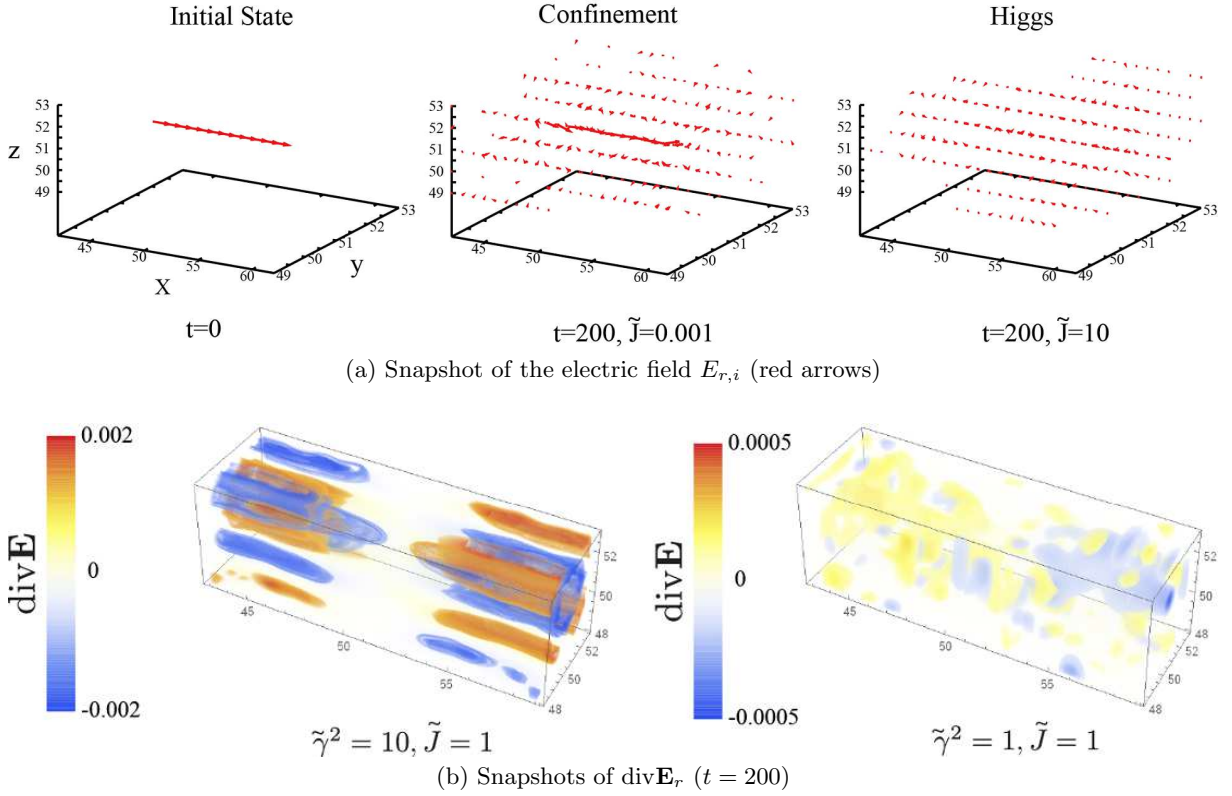


FIG. 9. (Color online) (a) Snapshots of the electric field $E_{r,i}$ for $\tilde{\gamma}^2 = 1$ with static charged sources pinned at r_{\pm} (See the text) with the flux length $\ell = 12$; (left) $t = 0$, (center) $t = 200$ for $\tilde{J} = 0.001$ (confinement regime), (right) $t = 200$ for $\tilde{J} = 10$ (Higgs regime). The electric flux spanned between static sources clearly survives for $\tilde{J} = 0.001$ and breaks for $\tilde{J} = 10$. (b) Snapshots of the divergence of electric field $\text{div} \mathbf{E}_r$ at $t = 200$ with the same static sources as (a). $\text{div} \mathbf{E}_r$ just measures the Higgs charge [See Eqs. (7) and (12)], and its magnitude is certainly larger for $\tilde{\gamma}^2 = 10$ (left) than for $\tilde{\gamma}^2 = 1$ (right).

$E_{r,i}$. Here, we fix the hopping parameter $J = 1$. The value of the density plot of $\text{div} \mathbf{E}_r$ for $\tilde{\gamma}^2 = 1$ is overall smaller than that for $\tilde{\gamma}^2 = 10$, that is, the Higgs charge in the weak Gauss-law coupling $\tilde{\gamma}^2 = 10$ is denser than the case $\tilde{\gamma}^2 = 1$. For $\tilde{\gamma}^2 = 10$, the distribution of $\text{div} \mathbf{E}_r$ appears a characteristic quasi-periodic structure. From these results in Fig. 9 lower line, the Gauss-law breaking $\text{div} \mathbf{E}_r \neq 0$ depends significantly on the parameter $\tilde{\gamma}^2$. This result is qualitatively in good agreement with the previous prediction Eq. (7) in Sec II. Also, this result implies that the Higgs charge tends to appear from the fluctuation due to the small Gauss-law coupling term, i.e, large $\tilde{\gamma}^2$, and that the fluctuating Higgs charges excite the surrounding electric fields. As a result, the initial electric flux may be disturbed and vanished.

V. PROPOSAL FOR FEASIBLE EXPERIMENT OF COLD ATOMIC GASES

In this section, we propose a feasible experimental setup for realization of a cold atom system on a BCT OL of Fig. 1, which is described by the EBHM of Eq. (1). Then, as explained in Sec. II, under certain conditions such as uniform and large average atomic density, this

atomic system is to be used to quantum-simulate the 3D GHM on a cubic GL. Theoretical investigation given in Sec. III and IV may be a guide for such experimental simulations.

It is possible to create a variety of lattice structure in 2D and 3D by appropriately arranging the propagation directions and the polarization of the laser beams [44, 45]. To prepare a BCT OL of Fig. 1, we follow the recent proposal by Boretz and Reichlof [46], and make use of the following optical potential;

$$V_{\text{BCT}} = u [\cos^2(k_1 x) + \cos^2(k_2 y) + \cos^2(k_3 z) + \cos(k_1 x) \cos(k_2 y) + \cos(k_2 y) \cos(k_3 z) + \cos(k_3 z) \cos(k_1 x)], \quad (25)$$

where $k_i = \pi/a_i$ ($a_1 = a_2 = a$, $a_3 = \sqrt{2}a$) and $x = n_1 a_1$, $y = n_2 a_2$ and $z = n_3 a_3$ with $n_i \in \mathbf{Z}$. The form of Eq. (25) can be produced by the standard method with three pairs of counterpropagating laser beams. We shall explain the coefficient u later [See Eq. (29)]. One may check that the minima of V_{BCT} for $u < 0$ are located at sites of the BCT lattice. More precisely, there are two groups of the minima; (i) $n_j \in 2m_j + 1$ ($m_j \in \mathbf{Z}$) corresponding to center sites of unit cells of the BCT lattice (as the sites 7, 8 in Fig. 1), and (ii) $n_j \in 2m_j$ to conner sites of unit

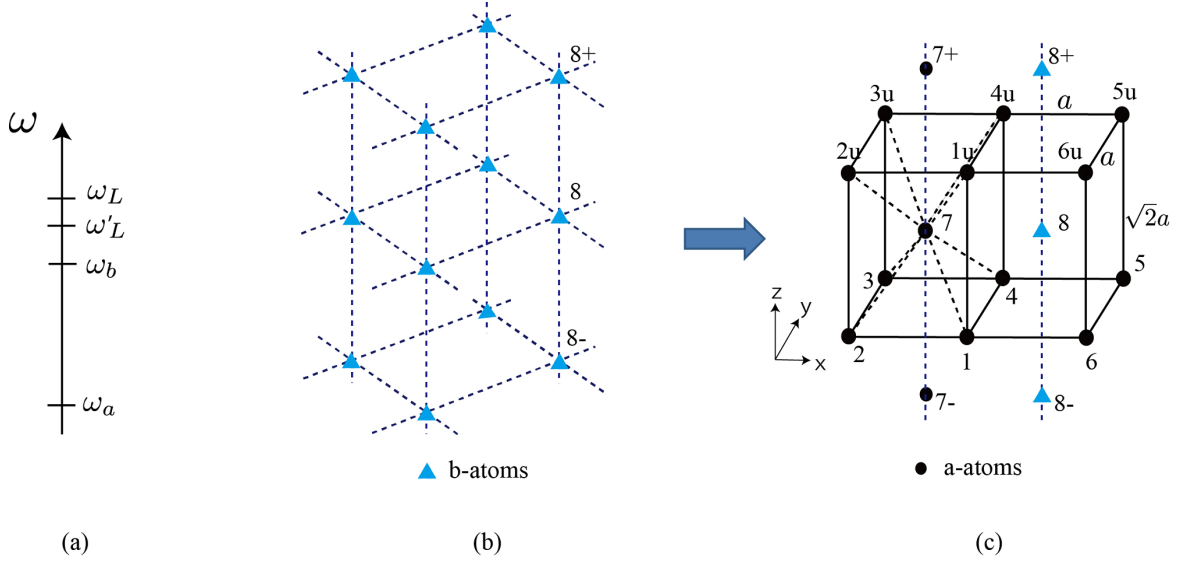


FIG. 10. (Color online) Setups to prepare the BCT OL of Fig. 1 with the interactions of Table I. (a) Choices of various frequencies ω 's appeared in the trapping potentials of Eqs. (25) and (28). (b) The cubic OL built by the potential V_{OCC} of Eq. (28). Its sites (marked by triangles) are odd-column centers (OCC) such as the sites 8, 8 $_{\pm}$ in Fig. 1, and occupied by b-atoms. (c) The BCT OL built after switching the trapping potential from V_{OCC} to V_{BCT} of Eq. (25). The a-atoms reside on its sites marked by black circles, while the b-atoms continue to occupy the OCC of (b).

cells (as 1~4, 1u~4u in Fig. 1).

To tune atomic interactions as in Table I, we propose the following two procedures;

(D1) We prohibit occupations of cold atoms on certain specific sites of the BCT OL. Explicitly, we exclude atoms from center sites of unit cells belonging to the odd-column $[(-)^{x+y} = -1]$ such as 8, 8 $_{\pm}$, and 8- in Fig. 1. In what follows, we call these excluded sites as odd-column centers (OCC). This certainly satisfies the condition for the group (iii) in Table I.

(D2) We adjust the parameters J_{ab} and V_{ab} so that the conditions for the groups (i), (ii), (iv), and (v) are satisfied. In fact, Rydberg atoms trapped on the OL [47] may have an isotropic interaction with a $1/r^3$ -type potential under certain external electric field [48]. This long-range interaction is expected to satisfy the condition in the groups (i, ii).

The condition for the NNN interactions in the groups (iv, v) may be satisfied (without relying upon dipole-dipole interactions) by making use of extended anisotropic orbitals of Wannier states in the excited bands of an optical lattice. In fact, this method was investigated explicitly in Ref. [24] to simulate the 2D GHM in a successful manner. We think that these methods are applicable also for the present 3D GHM without essential problems, and leave its details in a future publication.

Hereafter we focus our attention on the procedure (D1) above. A scenario for (D1) to exclude the atoms in question, which we call *a-atoms* hereafter, from OCC is by introducing another kind of atoms, which we call *b-atoms*, and let them reside only on the OCC and give them strong repulsion to repel the original a-atoms. The inter-

species interaction Hamiltonian \hat{H}_{ab} between a-atoms and b-atoms is given

$$\hat{H}_{ab} = U_{ab} \sum_{c \in \text{OCC}} \hat{\rho}_c \hat{n}_{bc}, \quad (26)$$

where c runs over the OCC, and \hat{n}_{bc} is the number operator of b-atoms residing on the site c . The b-bosons are assumed to be in a Mott state, so \hat{n}_{bc} may be approximated by a uniform mean value, $\hat{n}_{bc} \rightarrow \bar{n}_b$. Then we have

$$\hat{H}_{ab} \simeq U_{ab} \bar{n}_b \sum_{c \in \text{OCC}} \hat{\rho}_c. \quad (27)$$

For sufficiently large $U_{ab} \bar{n}_b$, the probability that a-bosons reside on the OCC is suppressed significantly.

From these consideration, we propose the following two steps to achieve the above procedure (D1);

1 Preparation of b-atoms on OCC.

Start with a continuum harmonic trapping system including both a-atoms and b-atoms. Prepare a 3D OL, the sites of which are just the OCC (See Fig. 10 (b)) and occupied by b-atoms. It is a simple cubic lattice with the lattice spacings $\sqrt{2}a$. The corresponding optical lattice potentials V'_a and V'_b felt by a-atoms and b-atoms respectively are given by

$$\begin{aligned} V'_{a(b)} &= u'_{a(b)} [\cos^2(k'_1 x) + \cos^2(k'_2 y) + \cos^2(k'_3 z)], \\ u'_{a(b)} &= -\frac{(d_{a(b)} E')^2}{\hbar \Delta'_{a(b)}} < 0, \\ k'_i &= \frac{\pi}{\sqrt{2}a}, \quad \Delta'_{a(b)} = \omega'_L - \omega_{a(b)}, \end{aligned} \quad (28)$$

where E' is the electric field strength induced by a standing laser, ω'_L is the laser frequency, $\omega_{a(b)}$ is the ns-np energy gap of a(b)-boson [49]. The amplitude $u'_{a(b)}$ is the result of the second-order perturbation of the electromagnetic interaction between the instantaneous dipole $\vec{d}'_{a(b)} = q_{a(b)}\vec{r}'_{a(b)}$ of a(b)-atoms and photons, $(d'_{a(b)}E')^2 \equiv \langle (\vec{d}'_{a(b)}\vec{E}')^2 \rangle$ [50]. $\Delta'_{a(b)}$ is a detuning parameter for the a(b)-atom fixed on blue detuning, $\Delta'_{a(b)} > 0$. We choose ω'_L in such a way that $\Delta'_b \ll \Delta'_a$ (See Fig. 10 (a)), so that the b-atoms are strongly trapped in OCC.

2 Changeover of optical potential.

Switch the laser potential from $V'_{a,b}$ of Eq. (28) to V_{BCT} of Eq. (25) within msec order. Because of the mixture of a-atoms and b-atoms, the amplitude u in V_{BCT} becomes u_a and u_b for a-atoms and b-atoms respectively, which are given by

$$u \rightarrow u_{a(b)} \equiv -\frac{(d'_{a(b)}E)^2}{\hbar\Delta_{a(b)}}, \quad \Delta_{a(b)} = \omega_L - \omega_{a(b)}, \quad (29)$$

where E and ω_L are parameters of the standing laser after the switch. As its time scale is smaller than typical time scale of quantum tunneling between neighboring wells (Fig. 10(b)), this potential changeover may prevent the b-atoms from escaping from OCC. Furthermore, by choosing ω_L so that

$$\Delta_b \ll \Delta_a \rightarrow |u_b| \gg |u_a|, \quad (30)$$

(See Fig. 10 (a)), the b-atoms continue to stay on OCC, even though the a-atoms are allowed to tunnel into nearest neighbor sites. We note that the

The resultant lattice system of a-atoms is shown in Fig. 10(c), which is described by H_{EBH} of Eq. (1). With the interaction parameters chosen according to the procedure (D2) above (and assuming $\bar{\rho}_0 \gg 1$), this a-atom system is just described by H'_{EBH} of Eq. (4) or equivalently by H_{GH} of Eq. (6).

VI. CONCLUSION

In this section, we summarize the results of the paper and present some outlooks. In Sec. II, we started from the EBHM in the 3D OL of Eq. (1), and derived its low-energy effective model Eq. (4) by assuming smallness of the density fluctuations $\hat{\eta}_a$ of atoms per site as $\langle \hat{\eta}_a \rangle / \rho_0 \ll 1$. This condition is satisfied not only for $\rho_0 \gg 1$ but also for $\rho_0 = O(1)$ as long as the excitation energy associated with $\hat{\eta}_a$ is sufficiently small. Then we show that this effective model becomes equivalent to the gauge-fixed version of the GHM in LGT when the interaction parameters J_{ab} and V_{ab} are suitable chosen as in Table I. This equivalence requires no special limit such as $\gamma \rightarrow 0$ owing to the inclusion of Higgs matter field.

We restricted ourselves to the region of J and γ^2 that supports a uniform (site-independent) average density,

$\langle \hat{\rho}_a \rangle = \rho_0$. For other region of parameters, the lowest-energy configuration favors inhomogeneous pattern of $\langle \hat{\rho}_a \rangle$ supporting density waves. In fact, in a separate paper [41], we consider the EBHM in one dimensional OL for general values of the on-sight repulsion V_0 and the NN repulsion $V \equiv V_{ab}$. Among other things, we study the phase diagram in the V_0 - V plane, and confirm that it certainly includes the density-wave phase in which $\langle \hat{\rho}_a \rangle$ takes two alternative values in every other sites. Even in such a case, the equivalence to the GHM is maintained in some region of V_0 and V by choosing J_{ab} and V_{ab} in a suitable manner.

In Sec. III, we studied the phase structure of the GHM by MC simulation. The explicit phase diagrams of Fig. 2 and Fig. 6 may work as a guide how to choose the model parameters in actual experiments of the system described by the EBHM. The coupling constants of the GHM are asymmetric in space-time directions in contrast to the LGT models studied in high-energy physics. This point may open a possibility of richer phase structure. The first-order phase transition found there is certainly such an example.

In Sec. IV, we studied the time development of the EBHM by using the semiclassical Gross-Pitaevskii type approach. Although the GPE underestimates the effect of quantum fluctuations and correlations, the obtained dynamical behavior of an electric field clearly changes as the coupling parameters change, reflecting the characteristics of each phase. The location of ‘‘phase boundary’’ determined by this way is qualitatively consistent with the result of the static MC simulation of Sec. III. These approximate but explicit and quantitative solutions of the dynamical equation certainly help us not only to design actual set up of experiments of quantum simulation, but also to get precise understanding of the real dynamics of gauge theory. For example, to understand the structure of potential of Fig. 8, simple shielding mechanism by pair creation of Higgs particles is not sufficient because the potential may saturate to a constant value when just a static Higgs pair is produced. Linear rising behavior at larger distance may be understood by taking the kinetic energy of Higgs bosons into account. This is done by the GPE which respects the energy conservation law.

In Sec. V, toward quantum simulation of the GHM, we present an explicit proposal to prepare an atomic system described by the EBHM. To realize the 3D GL, a BCT OL is a suitable configuration. To prevent the occupation on the OCC, one can use another kind of atoms to protect this occupation by the strong atom-atom repulsion. Adjustment of the NN and NNN interactions as in Table I seems to be a hard task, but engineering the atomic state into their higher-orbital state or arranging suitably the dipolar atoms or molecules can make desirable intersite interaction, which may lead to a realization of the parameter setting of Table I.

Our original aim is of course to simulate the target model, the GHM of LGT, by the base model, the EBHM of ultra cold atoms on the OL. However, the EBHM it-

self is an interesting model in theoretical viewpoint and our understandings of it is far from complete. Our static and dynamical study of the GHM made in this paper may be certainly of help to understand further the starting EBHM. Generally speaking, various notions and concepts established in LGT are to find their places in understanding ultra-cold atomic systems on OL, and vice versa. In fact, an explicit example of this mutual aid in one direction is discussed in Ref. [41], where the Haldane-insulator phase in the 1D EBHM is interpreted by LGT. By stretching one's imagination, in the opposite direction, the EBHM may shed some light to generalize LGT *beyond* the region of parameters where the present equivalence to LGT holds.

ACKNOWLEDGMENTS

Y. K. acknowledges the support of a Grant-in-Aid for JSPS Fellows (No.15J07370). This work was partially supported by Grant-in-Aid for Scientific Research from Japan Society for the Promotion of Science under Grant No. 26400246, 26400371 and 26400412.

Appendix A: Mean field calculation for the equilibrium atomic density in the 3D GL

In this appendix, we formulate a simple mean field theory (MFT) to calculate the mean value of the atomic density $\rho_a \equiv \langle \hat{\rho}_a \rangle$ in the 3D GL shown in Fig. 1, where the atoms are located on the links of the GL. In particular, we are interested in the competition between the homogeneous state in which ρ_a is a site-independent constant and the inhomogeneous state which has some periodic distribution and supports density-wave excitations.

To derive the energy E_{MFT} of MFT from H_{EBH} of Eq. (1), we first set $\exp(i\hat{\theta}_a) = 1$ ignoring the fluctuations of the phase $\hat{\theta}_a$, and replace the amplitude operator by its average as $\hat{\psi}_a \rightarrow \sqrt{\rho_a}$ and $\hat{\rho}_a \rightarrow \rho_a$. Then we obtain E_{MFT} including the chemical-potential term as

$$E_{\text{MFT}}(\rho) = - \sum_{a \neq b} J_{ab} \sqrt{\rho_a \rho_b} + \frac{V_0}{4} \sum_a \rho_a (\rho_a - 1) + \sum_{a \neq b} \frac{V_{ab}}{2} \rho_a \rho_b - \mu \sum_a \rho_a. \quad (\text{A1})$$

We consider the parameter setting shown in Table. I, E_{MFT} being then written as

$$E_{\text{MFT}}(\rho) = -J \sum_{a \neq b \in (\text{i,ii})} \sqrt{\rho_a \rho_b} + \frac{V_0}{4} \sum_a \rho_a (\rho_a - 1) + \frac{V}{2} \sum_{a \neq b \in (\text{i,ii,iv})} \rho_a \rho_b - \mu \sum_a \rho_a. \quad (\text{A2})$$

The chemical potential μ is chosen as a function of the mean density $\rho_0 = \sum_{a=1}^{N_s} \rho_a / N_s$ over the sites, so that the

total number of atoms in the system with $N_s (\equiv \sum_a 1)$ sites is a given number $N_s \rho_0$. In the case of homogeneous density, we can take $\rho_a = \rho_0$, which is site-independent. Using this ρ_0 , we rescale the energy as

$$\tilde{E}_{\text{MFT}}(\bar{\rho}) = \frac{E_{\text{MFT}}}{J \rho_0} = - \sum_{a \neq b \in (\text{i,ii})} \sqrt{\bar{\rho}_a \bar{\rho}_b} + \frac{V_0 \rho_0}{4J} \sum_a \bar{\rho}_a (\bar{\rho}_a - 1) + \frac{V \rho_0}{2J} \sum_{a \neq b \in (\text{i,ii,iv})} \bar{\rho}_a \bar{\rho}_b - \frac{\mu}{J} \sum_a \bar{\rho}_a. \quad (\text{A3})$$

Here, we have introduced the scaled density $\bar{\rho}_a = \rho_a / \rho_0$, so that $\bar{\rho}_a = 1$ for the homogeneous case. We minimize $\tilde{E}_{\text{MFT}}(\bar{\rho})$ with respect to $\bar{\rho}_a$ numerically to obtain an approximate configuration of $\bar{\rho}_a$ for the ground state.

Let us first consider the simplest case of vanishing NN and NNN couplings, $V = 0$ ($\gamma^2 = \infty$). Then the lowest-energy state with given ρ_0 is the uniform state $\bar{\rho}_a = \rho_0$. This is understood because inhomogeneous density fluctuations $\bar{\rho}_a = 1 + \delta \rho_a$ costs an extra energy ΔE as

$$\frac{\rho_0 V_0}{4J} \bar{\rho}_a (\bar{\rho}_a - 1) - \frac{\mu}{J} \bar{\rho}_a = \frac{\rho_0 V_0}{4J} [(\bar{\rho}_a - R)^2 - R^2],$$

$$R \equiv \frac{1}{2} + \frac{2\mu}{\rho_0 V_0},$$

$$\Delta E = \frac{\rho_0 V_0}{4J} \sum_a [(1 + \delta \rho_a - R)^2 - (1 - R)^2]$$

$$= \frac{\rho_0 V_0}{4J} \sum_a (\delta \rho_a)^2 > 0, \quad (\text{A4})$$

where $\sum_a \delta \rho_a = 0$ due to the total atomic-number conservation.

On the opposite case of vanishing on-site coupling $V_0 = 0$, the lowest energy state can be determined so as to minimize the inter-site coupling energy. Intuitively, this term dislikes the homogeneous density distribution, because, if we assume the alternative density undulation such as $\rho_a = \rho_0 + \delta \rho$ and $\rho_b = \rho_0 - \delta \rho$, simple inequality $(\rho_0 + \delta \rho)(\rho_0 - \delta \rho) = \rho_0^2 - (\delta \rho)^2 < \rho_0^2$ implies that the system prefers to the density wave state.

From these consideration we expect that the lowest energy state is homogeneous when the ratio of $V (= \gamma^{-2})$ and V_0 , $r \equiv V/V_0 = \gamma^{-2}/V_0$ is sufficiently small, while it becomes inhomogeneous as r becomes sufficiently large. To measure the degree of inhomogeneity of the lowest energy state, we use the following quantity m ,

$$m \equiv \frac{1}{N_s} \sum_{a=1}^{N_s} |\bar{\rho}_a - 1|, \quad (\text{A5})$$

which is zero for the homogeneous state and increases for the inhomogeneous one. The value of m can be calculated for general r and $V_0 \rho_0 / J$ by minimizing E_{MFT} numerically with respect to $\bar{\rho}_a$. In Fig. 11 we plot m as a function of r for several $V_0 \rho_0 / J$. It certainly supports our

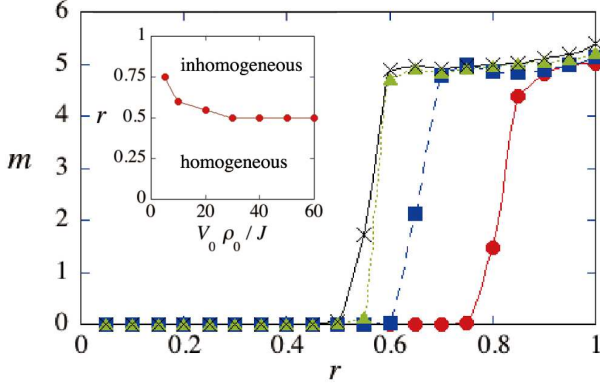


FIG. 11. Numerical result of the parameter m of Eq. (A5) as a function of the ratio of off-site and on-site repulsion, $r \equiv \gamma^{-2}/V_0$ for $\rho_0 V_0/J = 5$ (circles), 10 (squares), 20 (triangles), and 30 (crosses). The parameter m measures the nonuniformness of the ground state. The inset shows the parameter space showing the boundary between the homogeneous and inhomogeneous density distribution. For sufficiently large $\rho_0 V_0/J$, the density distribution of the ground state is homogeneous for $r \lesssim 0.5$, and it becomes inhomogeneous for $0.5 \lesssim r$.

expectation above. We note that, as the value $\rho_0 V_0/J$ increases, the critical ratio r saturates the value 0.5. From this result and the relation $V'_0 = V_0 - 2\gamma^{-2} = V_0(1 - 2r)$, positiveness of the electric energy ($V'_0 > 0$) implies the homogeneous ground state ($r < 0.5$) and vice versa. The inhomogeneous density distribution forms nontrivial patterns because of the intrinsic complexity of the 3D GL, which will be reported elsewhere.

Appendix B: Interpretation of the phase diagram

In this Appendix, let us discuss the global structure of Fig. 2, the phase diagram of 3D GHM given by Eq. (13), and interpret the order of transitions by a plausible argument.

First, we start to consider the case $c_2 = 0$. Then, the total action A_{GH} of Eq. (13) decouples to A_{I} of the time-like $\theta_{x,0}$ and A_{L} of the space-like $\theta_{x,i}$, and Z_{GH} becomes

$$\begin{aligned} Z_{\text{GH}}|_{c_2=0} &= (Z_{c_1})^{L^4} (Z_{3\text{DXY}})^L, \\ Z_{c_1} &= \int_{-\pi}^{\pi} \frac{d\theta}{2\pi} \exp(c_1 \cos \theta) = I_0(c_1), \\ Z_{3\text{DXY}} &= \int [D\theta_{r,i}] \exp \left[c_3 \sum_{r,i < j} \cos(\theta_{r,i} - \theta_{r,j}) + \dots \right]. \end{aligned} \quad (\text{B1})$$

The integrals over $[D\theta_{x,0}]$ decouples to L^4 sites, and each site gives rise to Z_{c_1} , the modified Bessel function. Z_{c_1} has no singularity in c_1 , and gives an average $\langle U_{x,0} \rangle = \langle \cos \theta_{x,0} \rangle = I_1(c_1)/I_0(c_1)$, which starts from 0 at $c_1 = 0$ and increases as c_1 increases up to 1. The integrals over

$[D\theta_{x,i}]$ decouples to L spatial 3D GL's labeled by x_0 , and each 3D system gives rise to $Z_{3\text{DXY}}$, the partition function of the 3D XY spin model. This is because the c_3 term in A_{GH} at fixed x_0 is just the energy of the NN XY spin model $E_{3\text{DXY}} = -c_3 \sum_{(a,b) \in (i)} \vec{S}_a \cdot \vec{S}_b$ of spins $\vec{S}_a = (\cos \theta_a, \sin \theta_a)$ defined on a 3D OL with the identification $\theta_{r,i} \leftrightarrow \theta_a$ as in Fig. 1 of Sec. II. $Z_{3\text{DXY}}$ is known to exhibit a second-order phase transition at $c_3 = c_{3c} \simeq 0.34$. For $c_3 > c_{3c}$ there is an order of $\theta_{r,i}$ and disorder otherwise. The horizontal second-order transition curve for $c_2 = 0$ in Fig. 2 expresses just this transition where the critical value of c_3 has no c_1 dependence because Z_{c_1} is analytic.

Next, we consider the effect of the c_2 term, A_{P} , which couples $\theta_{x,0}$ and $\theta_{x,i}$. In the mean-field type interpretation, one may decouple it as follows;

$$\begin{aligned} c_2 U_{x,0}^\dagger U_{x+0,i}^\dagger U_{x+i,0} U_{x,i} &\rightarrow c'_2 U_{x+0,i}^\dagger U_{x,i} + c''_2 U_{x,0}^\dagger U_{x+i,0}, \\ c'_2 &\equiv c_2 \langle U_{x,0}^\dagger U_{x+i,0} \rangle, \quad c''_2 \equiv c_2 \langle U_{x+0,i}^\dagger U_{x,i} \rangle. \end{aligned} \quad (\text{B2})$$

The first term in the R.H.S of Eq. (B2) is the NN pair of ‘‘XY’’ spin $U_{x,i}$ in the $\mu = 0$ direction with a ‘‘coupling constant’’ c'_2 . So this term and A_{L} compose a ‘‘pseudo’’ 4D XY model of XY spins $U_{x,i}$. Of course, this is not the genuine 4D XY model because its coupling c'_2 is ‘‘soft’’; it contains fluctuations of another variables $U_{x,0}$. For sufficiently large c_1 , the A_{I} term prepares a saturated value $\langle U_{x,0} \rangle \sim 1$ with small fluctuations. So c'_2 is almost a stable constant and the system becomes almost a genuine 4D XY model with asymmetric couplings (c_3, c'_2). This model is known to exhibit a second-order phase transition as its 3D counterpart irrespective of the value of \tilde{c}_3 as long as it is a constant. This explains the second-order transitions at large c_1 in Fig. 2. The second term of Eq. (B2) is the NN coupling of *time-like* XY spin $U_{x,0}$ in the 3D lattice at fixed x_0 with a soft ‘‘coupling constant’’, c''_2 . This gives rise to a set of L decoupled 3D XY spin models, each of which is labeled by x_0 . The term A_{I} works as an external source to $U_{x,0}$.

Therefore, the total system with the replacement (B2) is the sum of two subsystems; (i) one 4D XY model with coupling (c_3, c'_2) and (ii) L 3D XY models with coupling c''_2 and the source. Through the soft couplings c'_2, c''_2 these two subsystems affect each other. For example, let us start with the phase where both $U_{x,i}$ and $U_{x,0}$ are disordered, i.e., small c'_2, c''_2 . If c'_2 develops once by fluctuation, $U_{x,i}$ spins favor to order, which, in turn, may increase c''_2 and favors an order of $U_{x,0}$ and leads to larger c'_2 . That is, c'_2 and c''_2 rapidly increase each other by a synergistic effect. This is in strong contrast with usual ‘‘hard’’ coupling constants. As one changes usual constants c_1, c_3 with fixed c_2, c'_2 and c''_2 may not change linearly with c_1, c_3 , but keep zero until certain critical point and then rise continuously but abruptly. This behavior of soft couplings certainly brings the would-be second-order transition to a first-order transition. This is one explanation of the first-order transition shown in Fig. 2. The conditions to achieve the above scenario of first-order transitions are (i) sufficiently large c_2 and (ii) sufficiently small c_1 , be-

cause (i) c'_2 and c''_2 is proportional to c_2 and the above synergistic effect needs certain amount of sensitivity for each other, and (ii) if c_1 is large enough, $\langle U_{x,0} \rangle$ and hence c'_2 has small fluctuation and behaves as almost a "hard" constant.

Finally, let us make one comment on the above condition, (i) sufficiently large c_2 . If c_2 is too large, the couplings c'_2 and c''_2 may become stable enough, i.e., hard, and give rise to a second-order transition into a new phase

where both $\theta_{x,0}$ and $\theta_{x,i}$ are stable. For sufficiently small c_1 and c_3 , this new phase is certainly connected to the pure gauge theory without Higgs coupling, $c_1 = c_2 = 0$. Then this new phase is just the Coulomb phase which is characterized by the order of gauge field $\theta_{x,\mu}$ and disorder of Higgs field. Therefore, the present system may have a chance to exhibit the Coulomb phase. In fact, some preliminary MC simulations support this possibility. We shall report on this interesting possibility in future publication.

-
- [1] I. M. Georgescu, S. Ashhab, and F. Nori, *Rev. Mod. Phys.* **86**, 153 (2014).
- [2] M. Lewenstein, A. Sanpera, and V. Ahufinger, *Ultracold Atoms in Optical Lattices: Simulating Quantum Many-body Systems* (Oxford University Press, 2012).
- [3] I. Bloch, J. Dalibard, and S. Nascimbène, *Nat. Phys.* **8**, 267 (2012).
- [4] E. Zohar and B. Reznik, *Phys. Rev. Lett.* **107**, 275301 (2011).
- [5] E. Zohar, J. I. Cirac, and B. Reznik, *Phys. Rev. Lett.* **109**, 125302 (2012).
- [6] L. Tagliacozzo, A. Celi, A. Zamora, and M. Lewenstein, *Ann. Phys.* **330**, 160 (2013).
- [7] D. Banerjee, M. Dalmonte, M. Müller, E. Rico, P. Stebler, U.-J. Wiese, and P. Zoller, *Phys. Rev. Lett.* **109**, 175302 (2012).
- [8] E. Zohar, J. I. Cirac, and B. Reznik, *Phys. Rev. Lett.* **110**, 055302 (2013).
- [9] E. Zohar, J. I. Cirac, and B. Reznik, *Phys. Rev. Lett.* **110**, 125304 (2013).
- [10] D. Banerjee, M. Bögli, M. Dalmonte, E. Rico, P. Stebler, U.-J. Wiese, and P. Zoller, *Phys. Rev. Lett.* **110**, 125303 (2013).
- [11] L. Tagliacozzo, A. Celi, P. Orland, M. W. Mitchell, and M. Lewenstein, *Nat. Commun.* **4**, 2615 (2013).
- [12] E. Zohar, J. I. Cirac, and B. Reznik *Phys. Rev. A* **88**, 023617 (2013).
- [13] K. Kasamatsu, I. Ichinose, and T. Matsui, *Phys. Rev. Lett.* **111**, 115303 (2013).
- [14] U.-J. Wiese, *Annalen der Physik* **525**, 777 (2013).
- [15] E. Zohar, J. I. Cirac, B. Reznik, *Rep. Prog. Phys.* **79**, 014401 (2016).
- [16] A. Bazavov, Y. Meurice, S.-W. Tsai, J. Unmuth-Yockey, J. Zhang, *Phys. Rev. D* **92**, 076003 (2015).
- [17] K. Wilson, *Phys. Rev. D* **10**, 2445 (1974); J. B. Kogut, *Rev. Mod. Phys.* **51**, 659 (1979):
- [18] H. J. Rothe, *Lattice Gauge Theories: An Introduction*, World Scientific (2005).
- [19] I. Ichinose and T. Matsui, *Mod. Phys. Lett. B* **28**, 1430012 (2014).
- [20] Y. Takafuji, Y. Nakano, T. Matsui, *Physica A* **391**, 5285 (2012).
- [21] In Refs. [4, 5], it is proposed that one tunes the repulsive intersite interaction strength for nearest-neighbor sites and a subset of next-nearest neighbors to a common value γ^{-2} (See Table I and Eq. (12) in Sec. II) and takes the limit $\gamma^{-2} \rightarrow \infty$ ($\gamma^2 \rightarrow 0$).
- [22] We used MC simulations of the corresponding LGT defined on the 3+1-dimensional (3+1D) lattice where the extra one dimension is the imaginary-time axis in the path-integral representation of the zero-temperature partition function [17].
- [23] S. Baier, M. J. Mark, D. Petter, K. Aikawa, L. Chomaz, Z. Cai, M. Baranov, P. Zoller, and F. Ferlaino, *Science* **352**, 201 (2016).
- [24] Y. Kuno, K. Kasamatsu, Y. Takahashi, I. Ichinose, and T. Matsui, *New J. Phys.* **17**, 063005 (2015).
- [25] A. M. Polyakov, *Phys. Lett. B* **59**, 82 (1975).
- [26] A. Polkovnikov, S. Sachdev, S. M. Girvin, *Phys. Rev. A* **66**, 053607 (2002).
- [27] C. J. Pethick and H. Smith, *Bose-Einstein Condensation in Dilute Gases*, (Cambridge, 2008, second edition).
- [28] E. P. Gross, *Il Nuovo Cimento* **20**, 454(1961), L. P. Pitaevskii, *Soviet Physics JETP*. **13**, 451 (1961).
- [29] L. Pitaevskii and S. Stringari, *Bose-Einstein Condensation*, (Oxford, Oxford University Press, 2003).
- [30] For the case that V_{ab} of the group (iv) has a different value from γ^{-2} of the groups (i) and (ii), by repeating similar calculations we obtain still a model of LGT, but it contains long-range interactions between the vector potentials. It may be an interesting gauge theory worth to be studied, but we shall confine ourselves below to the standard gauge model with local interactions.
- [31] J. Kogut and L. Susskind, *Phys. Rev. D* **11**, 395 (1975). Here the relation between the pairs of vector potential and electric field, $A_i(\vec{r}), E_i(\vec{r})$ in the 3D continuum space and $\theta_{r,i}, E_{r,i}$ in a 3D cubic lattice, is given as the lattice spacing a' tends to zero as $\theta_{r,i} \rightarrow a'qA_i(\vec{r}), E_{r,i} \rightarrow (a')^2E_i(\vec{r})/(\hbar q)$, where q is the gauge coupling constant (charge unit). For the GL of Fig. 1, $a' = \sqrt{2}a$.
- [32] A comment is given on the value of quantized charge q of the Higgs field ϕ_x . In the Hamiltonian corresponding to the Wilson model [31], q appears, among other places, in the coefficient of the energy of electric field as $(q^2/a')\hat{E}_{x,i}^2$. If we apply this rule to H_{GH} of Eq. (6), we obtain the relation $V'_0/2 = q^2/(\sqrt{2}a)$. This, in turn, implies $q^2 = a/(\sqrt{2}c_2\Delta\tau)$. We note that the left-hand side of Gauss-law (7, 12) is expressed in terms of the integer-valued electric field $E_{r,i}$. The corresponding operator equation should read $\sum_i \nabla_i \hat{E}_{r,i} = \hat{a}_{r1}^\dagger \hat{a}_{r1} - \hat{a}_{r2}^\dagger \hat{a}_{r2}$ without the coefficient q , where $\hat{a}_{r1(2)}$ is the annihilation operator of Higgs (anti) particles [19]. The Higgs operator $\hat{\phi}_r$ which corresponds to ϕ_x in Eq. (16) (before taking the London limit) is expressed as $\hat{\phi}_r = [\hat{a}_{r1} + \hat{a}_{r1}^\dagger + i(\hat{a}_{r2} + \hat{a}_{r2}^\dagger)]/2$.
- [33] H. P. Büchler, M. Hermele, S. D. Huber, M. P. A. Fisher, and P. Zoller, *Phys. Rev. Lett.* **95**, 040402 (2005).

- [34] S. Tewari, V. W. Scarola, T. Senthil, and S. Das Sarma, Phys. Rev. Lett. **97**, 200401 (2006).
- [35] N. Metropolis, A. W. Rosenbluth, M. N. Rosenbluth, A. M. Teller, E. Teller, J. Chem. Phys. **21**, 1087 (1953).
- [36] Strictly speaking, in the case (iii), there remains a possibility of phase transition of infinite order such as Kosterlitz-Thouless transition.
- [37] B. Berg and T. Neuhaus, Phys. Rev. Lett. **68**, 9 (1992).
- [38] T. A. DeGrand and D. Toussaint, Phys. Rev. D **22**, 2478 (1980).
- [39] T. Pichler, M. Dalmonte, E. Rico, P. Zoller, and S. Montangero, Phys. Rev. X **6**, 011023 (2016).
- [40] A. Sinatra, C. Lobo, and Y. Castin, J. Phys. B At. Mol. Opt. Phys. **35**, 3599 (2002); A. Polkovnikov, Phys. Rev. A **68**, 053604 (2003); P. B. Blakie, A. S. Bradley, M. J. Davis, R. J. Ballagh, and C. W. Gardiner, Advances in Physics, **57**, 363 (2008).
- [41] Y. Kuno, K. Kawaki, S. Sakane, K. Kasamatsu, I. Ichinose, and T. Matsui, arXiv:1605.00333 (2016).
- [42] J. Schwinger, Phys. Rev. **714**, 16 (1951).
- [43] M. Endres, *Probing Correlated Quantum Many-Body Systems at the Single-Particle Level*, Springer Theses (2014), Chapter2.
- [44] K. I. Petsas, A. B. Coates, and G. Grynberg, Phys. Rev. A **50**, 5173 (1994).
- [45] P. Windpassinger and K. Sengstock, Rep. Prog. Phys. **76**, 086401 (2013).
- [46] Y. Boretz and L.E. Reichl, Phys. Rev. E **91**, 042901 (2015).
- [47] S. E. Anderson, K. C. Younge, and G. Raithel, Phys. Rev. Lett. **107**, 263001 (2011).
- [48] H. P. Buchler, A. Micheli, and P. Zoller, Nat. Phys. **3**, 726 (2007); R. Heidemann, U. Raitzsch, V. Bendkowsky, B. Butscher, R. Low, and T. Pfau, Phys. Rev. Lett. **100**, 033601 (2008).
- [49] R. Graham, M. Schlautmann, and P. Zoller, Phys. Rev. A **45**, R19(R) (1992).
- [50] D. Jaksch, and P. Zoller, Ann. Phys. (N.Y.) **315**, 52 (2005).